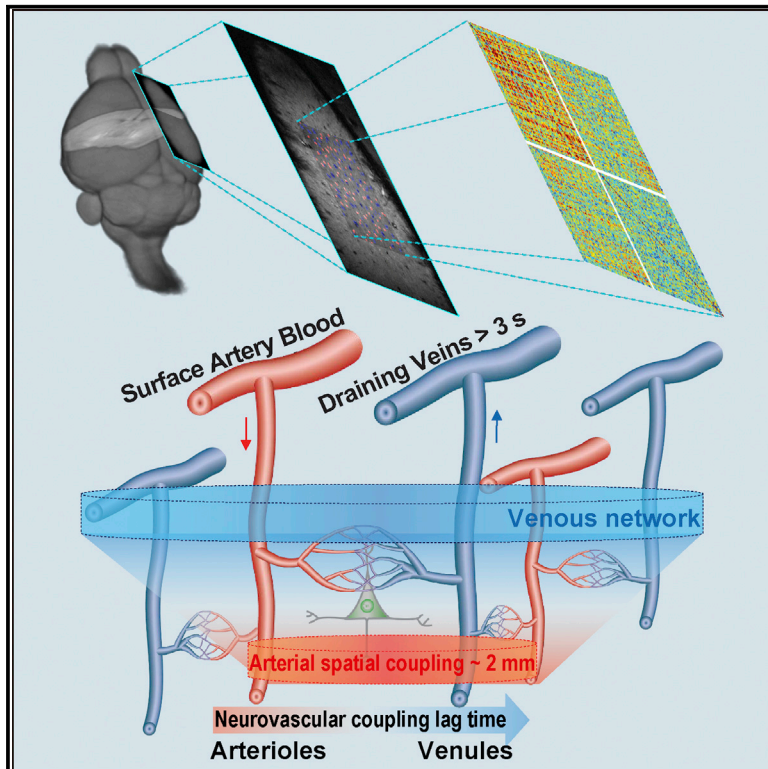


# Neuron

## Ultra-Slow Single-Vessel BOLD and CBV-Based fMRI Spatiotemporal Dynamics and Their Correlation with Neuronal Intracellular Calcium Signals

### Graphical Abstract



### Authors

Yi He, Maosen Wang, Xuming Chen, ..., Bruce R. Rosen, David Kleinfeld, Xin Yu

### Correspondence

xin.yu@tuebingen.mpg.de

### In Brief

He et al. performed single-vessel fMRI in rat to map spatiotemporal correlations of ultra-slow arteriole CBV and venule BOLD fluctuations, concurrent with intracellular-calcium photometry. They find a 2 mm correlation length, which bears on the resolution of functional connectivity.

### Highlights

- bSSFP-based single-vessel fMRI reveals dynamic vascular network connectivity
- Arterioles and venules showed distinct patterns of spatiotemporal correlations
- Neural  $\text{Ca}^{2+}$  ultra-slow oscillations correlate to vessel-specific fMRI fluctuations
- Human brain fMRI signal fluctuations were mapped in individual gray matter veins

# Ultra-Slow Single-Vessel BOLD and CBV-Based fMRI Spatiotemporal Dynamics and Their Correlation with Neuronal Intracellular Calcium Signals

Yi He,<sup>1,2</sup> Maosen Wang,<sup>1,2</sup> Xuming Chen,<sup>1,2</sup> Rolf Pohmann,<sup>1</sup> Jonathan R. Polimeni,<sup>3</sup> Klaus Scheffler,<sup>1,6</sup> Bruce R. Rosen,<sup>3</sup> David Kleinfeld,<sup>4,5</sup> and Xin Yu<sup>1,7,\*</sup>

<sup>1</sup>High-Field Magnetic Resonance Department, Max Planck Institute for Biological Cybernetics, 72076 Tuebingen, Germany

<sup>2</sup>Graduate Training Centre of Neuroscience, International Max Planck Research School, University of Tuebingen, 72074 Tuebingen, Germany

<sup>3</sup>MGH/MIT/HMS Athinoula A. Martinos Center for Biomedical Imaging, Department of Radiology, Harvard Medical School, Massachusetts General Hospital, Charlestown, MA 02114, USA

<sup>4</sup>Department of Physics

<sup>5</sup>Section of Neurobiology

University of California at San Diego, La Jolla, CA 92093, USA

<sup>6</sup>Department of Biomedical Magnetic Resonance, University of Tübingen, 72076 Tübingen, Germany

<sup>7</sup>Lead Contact

\*Correspondence: [xin.yu@tuebingen.mpg.de](mailto:xin.yu@tuebingen.mpg.de)

<https://doi.org/10.1016/j.neuron.2018.01.025>

## SUMMARY

Functional MRI has been used to map brain activity and functional connectivity based on the strength and temporal coherence of neurovascular-coupled hemodynamic signals. Here, single-vessel fMRI reveals vessel-specific correlation patterns in both rodents and humans. In anesthetized rats, fluctuations in the vessel-specific fMRI signal are correlated with the intracellular calcium signal measured in neighboring neurons. Further, the blood-oxygen-level-dependent (BOLD) signal from individual venules and the cerebral-blood-volume signal from individual arterioles show correlations at ultra-slow (<0.1 Hz), anesthetic-modulated rhythms. These data support a model that links neuronal activity to intrinsic oscillations in the cerebral vasculature, with a spatial correlation length of ~2 mm for arterioles. In complementary data from awake human subjects, the BOLD signal is spatially correlated among sulcus veins and specified intracortical veins of the visual cortex at similar ultra-slow rhythms. These data support the use of fMRI to resolve functional connectivity at the level of single vessels.

## INTRODUCTION

The cerebral vasculature is an interconnected network that supplies metabolites to the brain and mediates chemical signaling between the brain and the body. Cerebral circulation is mediated by an electrogenic vascular system, composed of interconnected endothelial cells that transmit signals between neighboring vessels to control the tone of arteriole smooth muscle (Ay-

din et al., 1991; Longden et al., 2017) in addition to forming the lumen of the vessels. The vascular system exhibits a number of rhythms of neurological and vascular origin (Obrig et al., 2000; Tak et al., 2015; Zhu et al., 2015). Respiratory- and cardiac-based rhythmic components can be regressed out of the fMRI data. Yet an ultra-low frequency (0.1 Hz) fluctuation in the diameter of arterioles, known as vasomotion (Intaglietta, 1990), remain. Far from a confounding factor (Murphy et al., 2013), these fluctuations form the basis of resting-state fMRI (Biswal et al., 1995; Fox and Raichle, 2007). Critically, vasomotion has been shown to be entrained by similarly ultra-slow oscillations in neuronal signaling (Mateo et al., 2017). It has been hypothesized that these covaried vasomotion and oscillatory neuronal patterns may contribute to the physiological basis of the resting-state fMRI connectivity mapping. This would provide the underpinning to observations of concurrent ultra-slow neuronal and hemodynamic signals, acquired optically (Schulz et al., 2012; Du et al., 2014; Ma et al., 2016) and electrophysiologically (Shmuel and Leopold, 2008; Schölvinck et al., 2010).

It is an open challenge to merge the optically acquired neuronal and vessel-specific hemodynamic signaling events with fMRI recordings to directly interpret the vascular basis of the resting-state fMRI signal (Logothetis et al., 2001). In most past work, the resting-state fMRI signal is acquired from large brain voxels (He et al., 2008; Shmuel and Leopold, 2008; Schölvinck et al., 2010). However, more recently high-resolution fMRI has allowed us to map vessel-specific hemodynamic signal from distinct vessel-dominated versus parenchyma-dominated voxels enriched with capillaries in animal brains with either cerebral blood volume (CBV) fMRI or blood-oxygen-level-dependent BOLD (fMRI) (Yu et al., 2012; Moon et al., 2013; Poplawsky et al., 2017). Using line-scanning fMRI methods, the iron oxide particle-based CBV-weighted signal is localized at penetrating arterioles (Yu et al., 2016), while the BOLD signal is detected at penetrating venules (Mansfield et al., 1976; Silva and Koretsky, 2002; Yu et al., 2012, 2014). Thus, the high-resolution fMRI will

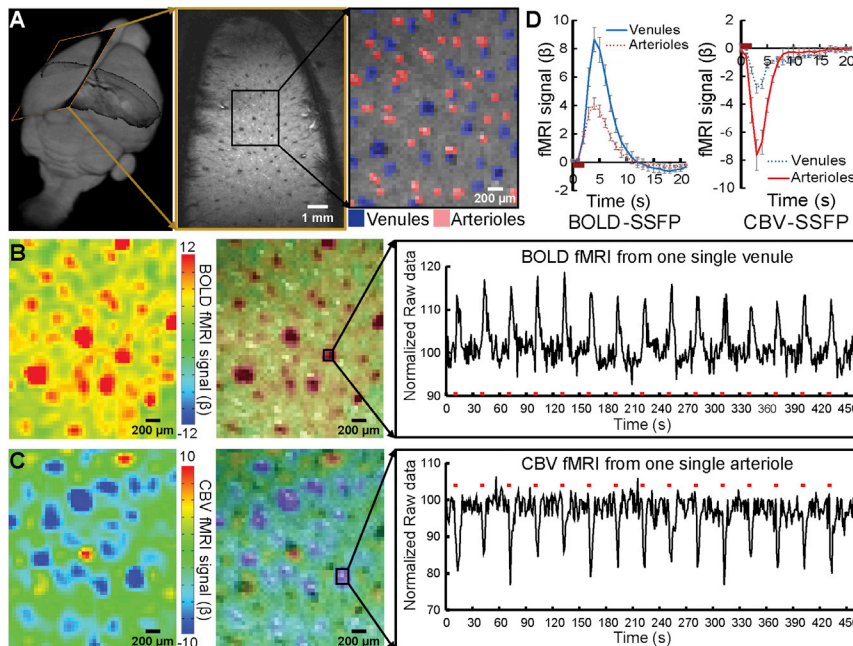


**Figure 1. Balanced Steady-State Free Precession-Based Task-Related Single-Vessel BOLD and CBV fMRI**

(A) An A-V map shows individual venules (dark dots, blue markers) and arterioles (bright dots, red markers) in a 2D slice.

(B) The BOLD fMRI map (left) and the semi-transparent map overlaid on the A-V map demonstrate the venule-dominated peak BOLD signal with the on/off block time series from a single venule ROI.

(C) The CBV fMRI map (left) and the semi-transparent map overlaid on the A-V map show the arteriole-dominated peak CBV signal with the on/off block time series from a single arteriole ROI.

(D) The averaged BOLD (left)/CBV (right) fMRI response function from venule (blue) and arteriole (red) voxels ( $n = 5$ , mean  $\pm$  SEM). See also [Figures S1](#) and [S4](#) and [Table S1](#).

permit us to follow neurovascular-coupled hemodynamic signals as they propagate from the arteriolar network, e.g., in terms of a CBV-weighted signal that will be sensitive to changes in vascular diameter, to the venous network, e.g., in terms of the BOLD signal, to gain a vascular-specific view of hemodynamic signaling with fMRI.

The technical goal of this work is 2-fold. The first is to detect the vessel-specific fluctuations in fMRI signals during the resting state. This goal must be accomplished across a plane through cortex with sufficient speed to accurately determine the magnitude and phase of correlation mediated by vasomotor fluctuations across vessels. The second is to measure these fluctuations concurrent with calcium signal recordings from neighboring neurons. Our approach builds on our ability to identify brain arterioles from venules with MRI and our line-scanning method to map the single-vessel hemodynamic signal (Yu et al., 2016). The line-scanning scheme reshuffled the k-space acquisition so that each image was reconstructed from data acquired along the entire experimental time series with a fast sampling rate, but not in real time (Silva and Koretsky, 2002; Yu et al., 2016). Here, we develop a single-vessel resting-state fMRI mapping method to specify the unique temporal dynamic features of neurovascular oscillatory signals, as well as to characterize the spatial distribution of fluctuations in the fMRI signal in both arteriolar and venous networks. We ask: (1) can the balanced steady-state free precession (bSSFP) method be used to detect vessel-specific fMRI signal fluctuations during resting state? The bSSFP method has higher SNR per time unit than the line-scanning method and presents less image distortion with reduced extravascular effect than the echo-planar imaging (EPI) method for high-field rat brain fMRI (Scheffler and Lehnardt, 2003). (2) Can both BOLD and CBV signals be detected at the scale of penetrating vessels, the finest spatial scale within the brain in

cortical vessels studied with fMRI match all or part of the fMRI signal with the context of low-frequency fluctuations in brain state (Schulz et al., 2012; Du et al., 2014; Ma et al., 2016)? (4) Lastly, can the single-vessel fMRI scheme be extended to map the vessel-specific long-range correlation patterns in the gray matter of the human brain?

## RESULTS

### Single-Vessel Mapping of the Evoked BOLD and CBV-Weighted Signal with bSSFP-fMRI

Balanced steady-state free precession (bSSFP) single-vessel fMRI was implemented to map the evoked BOLD and CBV-weighted fMRI signal in the forepaw region of primary sensory (S1) cortex rats under  $\alpha$ -chloralose anesthesia. Although anesthesia will alter brain rhythms, and lower the ultra-slow fluctuations to below their awake, resting-state value of  $\sim 0.1$  Hz (Chan et al., 2015), the use of anesthesia is currently necessary for stability in these initial single-vessel fMRI measurements. Our stimulus was transient electrical stimulation of the forepaw. To acquire a high spatial resolution 2D bSSFP image, we acquired each spin echo every 7.8 ms to shorten the total acquisition time for each 2D image, comprising a  $96 \times 128$  matrix (FOV,  $9.6 \times 12.8$  mm) for an in-plane resolution of  $100 \times 100 \mu\text{m}$ , to a TR of 1 s. As described previously (Yu et al., 2016), a multi-gradient-echo (MGE) sequence was used to distinguish among individual arterioles (bright dots, due to the inflow effect) and venules (dark dots, due to fast  $T_2^*$  decay of deoxygenated blood) from the anatomical single-vessel 2D images, i.e., the arteriole-venule (A-V) map (Figure 1A). Also noteworthy is that the A-V ratio is  $0.85 \pm 0.04$  (Table S1), demonstrating more penetrating veins than arteries, which is consistent with what has been previously reported in rodents (Hirsch et al., 2012; Blinder et al., 2013).

Further, the sensory-evoked single-vessel BOLD and CBV-weighted fMRI signal was detected by the bSSFP single-vessel fMRI before and after iron oxide particle injection. The data of Figure 1B show that the peak BOLD signals are primarily located at the venule voxels with the time course of the positive BOLD signal from a selected venule (Figure S1). After an injection of iron oxide particles, the bSSFP fMRI signal was acquired in the same 2D slice and shows that the evoked CBV-weighted signal corresponds to a decreased T2\*-weighted MR signal (Figure 1C). Note that the T2\*-weighted signal drops since activity-evoked vasodilation leads to an increased blood volume with more iron oxide particles in a given voxel, which shortens the magnitude of T2\* and diminishes the signal (Mandeville et al., 1998). The peak CBV-weighted signal was mainly located at individual arterioles with the time course of the negative CBV-weighted signal originated from a selected arteriole (Figures 1C and S1). The averaged hemodynamic time courses from regions of interest of venule and arteriole voxels showed that the positive BOLD signal is much higher in venule than arteriole voxels (Figure 1D). Similarly, the negative CBV-weighted signal is much lower in arteriole than venule voxels (Figure 1D). Interestingly, the CBV-weighted signal in arteriole voxels returned to baseline faster than that in venules. An extended temporal response for the CBV-weighted signal in venules has been previously reported for CBV-based fMRI studies (Mandeville et al., 1999; Silva et al., 2007; Drew et al., 2011) and may be inferred from optical imaging (Drew et al., 2011). These results demonstrate the feasibility of bSSFP-fMRI for real-time single-vessel hemodynamic mapping from arterioles. They complement the venule-dominated approach for the positive BOLD signal mainly in terms of oxy/deoxy-hemoglobin ratio changes.

### Single-Vessel bSSFP fMRI Mapping the Resting-State BOLD and CBV-Weighted Signals

Moving beyond the evoked single-vessel fMRI mapping, the ultra-slow resting-state hemodynamic signal was directly mapped with the bSSFP single-vessel fMRI method. Individual arterioles or venules identified from the A-V map were selected as seed voxels to calculate the correlation maps of both BOLD and CBV-based fluctuations in the fMRI signal (Figure 2); the frequency range was 0.01 to 0.1 Hz. As shown in the example data of Figure 2B, venule voxels were highly correlated to each other but less correlated for arterioles in the resting-state BOLD correlation maps (Movie S1). In contrast, as shown in the example data of Figure 2C, arteriole voxels were highly correlated but venules essentially uncorrelated in the resting-state CBV-weighted correlation maps (Movie S2). The power spectral density shows that the venule-specific BOLD and arteriole-specific CBV-weighted fMRI signal fluctuate within the ultra-slow frequency range of 0.01 to 0.04 Hz (Figure 2D). Similar to the evoked fMRI maps, the significant BOLD signal correlations were primarily located at venule voxels, i.e., the venule-specific connectivity map, and the significant CBV-weighted signal correlation were primarily located at arteriole voxels, i.e., the arteriole-specific connectivity map, during the resting state.

To better characterize the spatial and temporal features of the single-vessel fMRI fluctuations, the vessels identified in

the A-V map were paired to calculate correlation coefficients (Figure 3A). First, the values of the correlation coefficient for all vessel pairs (arteriole pairs: A-A; venule pairs: V-V) were plotted as the function of inter-vessel distance. For the BOLD signal fluctuation, V-V pairs show a stronger correlation than that of A-A pairs in the large field-of-view, up to  $5 \times 5$  mm. This highlights the large-scale extent of the BOLD-based venule functional connectivity (Figures 3B and 3F). In contrast to the case for BOLD, a stronger correlation was detected for the A-A pairs than the V-V pairs for the CBV-weighted signal fluctuations. These correlations diminished over a vessel separation distance of 2 mm (Figures 3C and 3G). This spatial scale is consistent with the scale for correlations in vasomotion across arterioles, as detected by two-photon imaging of vessel diameter (Mateo et al., 2017). This spatial scale also corresponds to the  $\sim 2$  mm electrotonic length for conduction through endothelial cells (Segal and Duling, 1989). The color-coded correlation matrices showed higher BOLD values of correlation in V-V pairs than the other pairs (Figure 3D) and higher CBV-weighted values of correlation in A-A pairs than the other pairs (Figure 3E), which is quantitatively represented as the function of vessel pair distance (Figures 3F and 3G).

Next, Spectral coherence analysis from paired venules or arterioles was performed to characterize the full frequency spectrum of the vessel-specific fMRI signal fluctuation during the resting state. The coherent oscillation was mainly distributed in the 0.01–0.04 Hz frequency range for both BOLD and CBV-weighted fMRI signal fluctuation (Figures 3H and 3I, similar to the spectral power, Figure 2D). Quantitative analysis demonstrates that the coherence coefficient of venule pairs is significantly higher than that of arteriole pairs for the BOLD signal fluctuation. In contrast, for the CBV-weighted signal fluctuation, the coherence coefficient of arteriole pairs is significantly higher than that of venule pairs for the 0.01–0.04 Hz frequency bandwidth (Figures 3J and 3K). In addition to the seed-based analysis, independent component analysis (ICA) was used to determine the venule-specific dynamic connectivity for BOLD signal fluctuation and the arteriole-specific dynamic connectivity for CBV-weighted signal fluctuation (Figures S2A–S2G). One component appeared specific for vessel-specific BOLD ultra-slow oscillations and another for CBV-weighted the ultra-slow oscillations (Figures S2F and S2G). These results confirm distinct vessel-specific correlation patterns for BOLD and CBV-weighted signal fluctuation.

Vessel-specific BOLD correlation maps were detected in rats anesthetized with isoflurane ( $<1.2\%$  [v/v]) (Figures S2H–S2M). The frequency range of oscillations extended to  $\sim 0.1$  Hz with peak power levels at 0.01–0.04 Hz, similar to those observed with rats anesthetized with  $\alpha$ -chloralose (Figure 2). This result suggests that while oscillation at frequencies above  $\sim 0.1$  Hz may vary depending on the anesthetized or awake brain state (Obrig et al., 2000; Du et al., 2014; Ma et al., 2016; Mateo et al., 2017), the ultra-slow frequencies are fairly stable ( $<0.1$  Hz) under uniform ventilation. It is noteworthy that blood pressure was acquired simultaneously with fMRI, but no clear ultra-slow frequency fluctuation was observed from either of the physiological parameters (Figure S3).

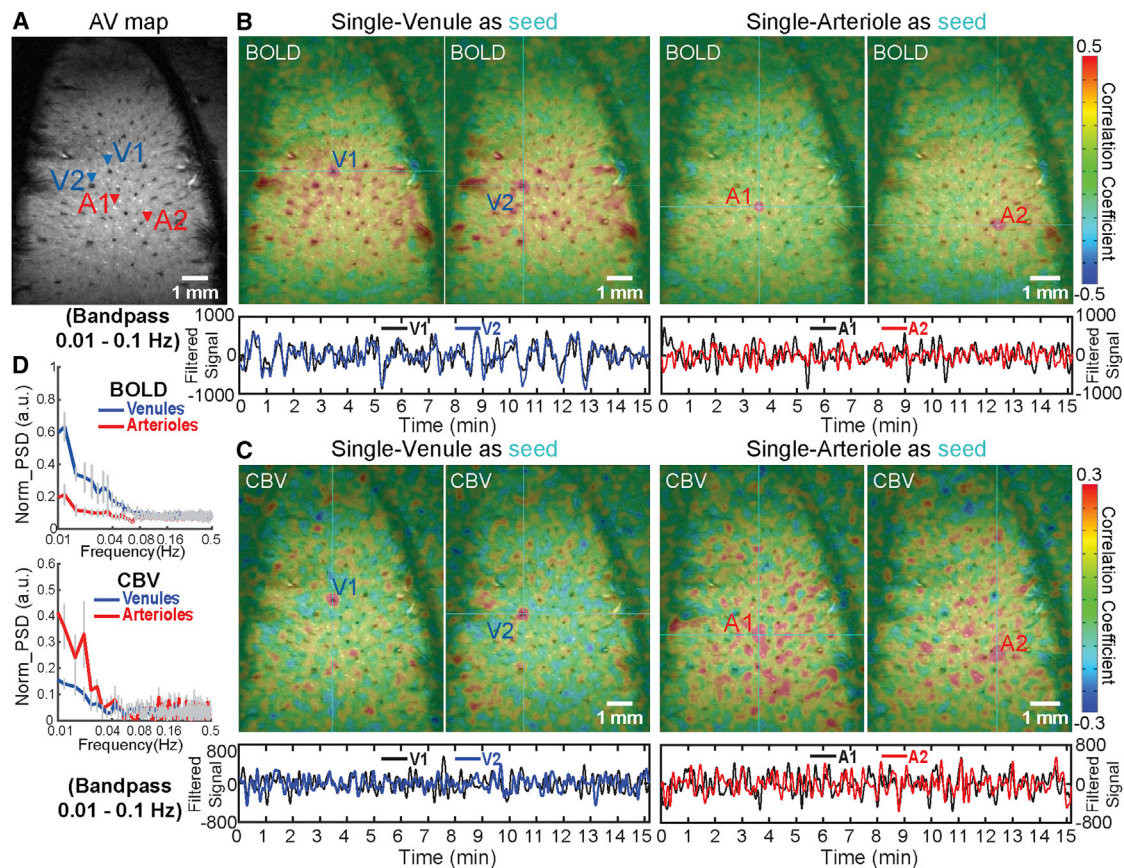


**Figure 2. Using bSSFP-Based rs-fMRI to Map Vascular-Specific Correlation Patterns**

(A) The A-V map shows individual penetrating arterioles and venules (blue arrowheads, venules; red arrowheads, arterioles). (B) The seed-based BOLD rs-fMRI correlation maps (0.01–0.1 Hz; seeds: cyan crosshairs) of two venule seeds (V1 and V2; left) and CBV rs-fMRI correlation maps (0.01–0.1 Hz; seeds: cyan crosshairs) of two arteriole seeds (A1 and A2; right). The lower panel is the BOLD signal time course of the two venule seed ROIs and two arteriole seed ROIs. (C) The seed-based CBV rs-fMRI correlation maps (0.01–0.1 Hz; seeds: cyan crosshairs) of two venule seeds (V1 and V2; left) and CBV rs-fMRI correlation maps (0.01–0.1 Hz; seeds: cyan crosshairs) of two arteriole seeds (A1 and A2; right). The lower panel is the CBV signal time course of the two venule seed ROIs and two arteriole seed ROIs. (D) The power spectral density (PSD: arbitrary unit [a.u.]) of the venule and arteriole-specific resting-state BOLD (upper) and CBV (lower) fMRI time courses. See also [Figures S2](#) and [S3](#).

### Comparison of Vessel-Specific BOLD and CBV fMRI Signals with Simultaneous Neuronal Calcium Recording

To characterize the potential neural correlates of the vessel-specific fMRI signal fluctuation, a genetically encoded calcium indicator, GCaMP6f, was expressed in neurons of forepaw S1 or vibrissa S1 cortex for simultaneous intracellular  $[Ca^{2+}]$  recording and fMRI ([Figure S4](#)); immunostaining verified the GCaMP expression in cortical neurons ([Figure S4B](#)). Evoked and spontaneous intracellular  $[Ca^{2+}]$  transients were recorded in the deep layers with fiber photometry concurrent with the local field potential (LFP) ([Figures 4A](#) and [S4C–S4F](#)). Evoked  $[Ca^{2+}]$  spikes were acquired simultaneously with single-vessel bSSFP-fMRI for comparison with the venule-specific positive BOLD signal and arteriole-specific negative CBV-weighted signal ([Figures S4E](#) and [S4F](#)). These results demonstrate the feasibility of simultaneous single-vessel fMRI with intracellular  $[Ca^{2+}]$  fiber optic recording.

We sought to characterize the potential neuronal origin of the vessel-specific fMRI signal fluctuation. We first considered the correlation between changes in intracellular  $[Ca^{2+}]$  in the 0.01 to 0.1 Hz band and the resting-state BOLD signal. It shows vessel-specific positive correlation patterns that are similar to the venule-seed based correlation maps from rats anesthetized with  $\alpha$ -chloralose ([Figures 4B](#) and [4C](#)); time courses of representative venules (V1, V2), and changes in intracellular  $[Ca^{2+}]$  are shown in [Figure 4D](#). The correlation coefficient between the intracellular  $[Ca^{2+}]$  and the venule BOLD signal ( $Ca^{2+}$ -V) was significantly higher than that with the arteriole BOLD signal ( $Ca^{2+}$ -A) ([Figure 4F](#)). Cross-correlation analysis between the changes in intracellular  $[Ca^{2+}]$  and the venule-specific BOLD signal showed a positive peak at the averaged lag time of  $2.3 \pm 0.2$  s ([Figures 4E](#) and [4G](#)). The vessels at the cortical surface had the longest lag, up to 3–5 s ([Figure 4C](#)), which agrees with the lag reported previously by cross-correlation analysis of the

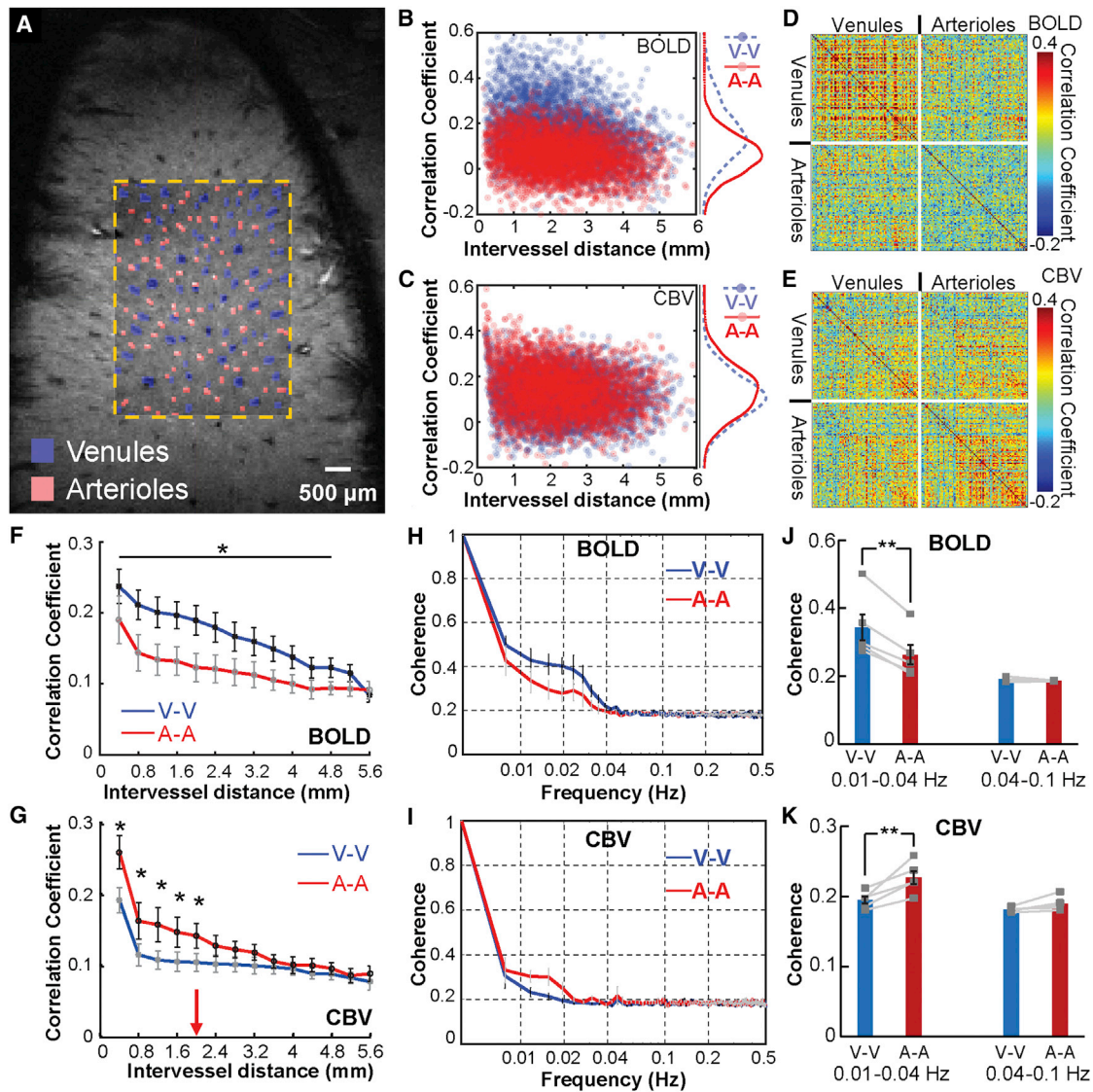


**Figure 3. Vascular Dynamic Network Connectivity in Rats at 14.1T**

(A) The A-V map of one representative rat (arteriole ROIs in red and venule ROIs in blue).

(B and C) Scatterplots of the correlation coefficient (CC) of BOLD (B) and CBV (C) fMRI from venule-to-venule (V-V) pairs, arteriole-to-arteriole (A-A) pairs as the function of the inter-vessel distance from one representative rat.

(D and E) The correlation matrices of all vessel pairs for the BOLD (D) and CBV (E) fMRI from one representative rat.

(F and G) The mean CC value of the BOLD signal from the venule pairs is significantly higher than that of the arteriole pairs with large spatial inter-vessel distance ( $>5$  mm) (F,  $n = 5$ , mean  $\pm$  SEM, \*, paired t test,  $p < 0.03$ ). In contrast, the mean CC value of the CBV signal from the arteriole pairs is significantly higher than that of the venule pairs with small spatial inter-vessel distance ( $\sim 2$  mm) (G,  $n = 5$ , mean  $\pm$  SEM, \*, paired t test,  $p < 0.03$ ).

(H and I) The averaged coherence graph of paired venules and arterioles from BOLD/CBV fMRI (H), BOLD fMRI,  $n = 5$ , (I), CBV fMRI,  $n = 5$  rats, mean  $\pm$  SEM.

(J) The mean BOLD coherence coefficient of the venule pairs is significantly higher than that of arteriole pairs at the low-frequency range (0.01–0.04 Hz) ( $n = 5$ , paired t test, \*\* $p = 0.0009$ ).

(K) The mean CBV coherence value of paired venules is significantly lower than that of paired arterioles at the low-frequency range (0.01–0.04 Hz) ( $n = 5$  rats, paired t test, \*\* $p = 0.007$ ).

See also [Figures S2](#) and [S3](#).

calcium signal and hemoglobin-based intrinsic optical signal (Du et al., 2014).

We next considered the correlation of the calcium signal in the 0.01–0.1 Hz band with the single-vessel CBV-weighted fMRI signal obtained after the injection of iron oxide particles. Similar

to the arteriole-seed based CBV correlation maps (Figure 4I), the highly correlated voxels with changes in intracellular  $[Ca^{2+}]$  were located mainly at arterioles, but with negative values of the correlation coefficient (Figure 4J); the time courses of representative arterioles (A1, A2) and the calcium signal are shown in Figure 4K.

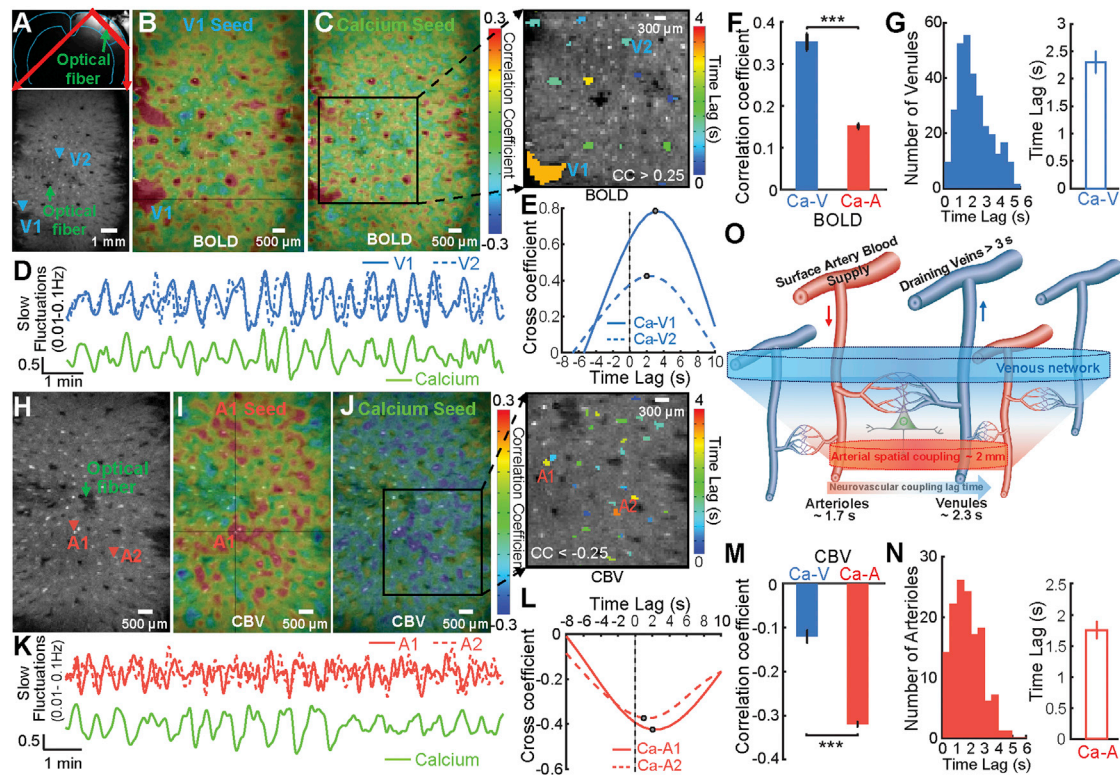


**Figure 4. Correlation Analysis of the Single-Vessel BOLD/CBV fMRI with GCaMP6f-Mediated Calcium Signal**

(A) The coronal view of the anatomical MR image with the optic fiber targeting the vibrissa S1 (upper). The A-V map from a 2D slice covering the deep cortical layer (lower).

(B) The seed-based BOLD correlation maps from one representative venule voxels (V1) overlaid on the A-V map.

(C) The correlation map between the BOLD fMRI signal and the calcium signal (band-pass filter: 0.01–0.1 Hz). Inset is a representative color-coded lag time map between the calcium signal with the BOLD fMRI of individual venules ( $CC > 0.25$ ).

(D) The time courses of the BOLD fMRI signal from vessel voxels (V1: blue, solid line; V2: blue, dotted line) and the slow oscillation calcium signal (green).

(E) The cross-correlation function of the calcium signal and BOLD fMRI signal of two representative venules (Ca-V1 and Ca-V2) with positive peak coefficients at the lag time 2–3 s.

(F) The mean correlation coefficient of the calcium signal with the BOLD fMRI signal of venules is significantly higher than that of arterioles ( $n = 7$  rats, mean  $\pm$  SEM, paired t test,  $***p = 2.5 \times 10^{-5}$ ).

(G) The histogram of venules with lag times varied from 0.5 to 6 s ( $CC > 0.25$ ) and mean lag time at  $2.30 \pm 0.19$  s. ( $n = 7$ , mean  $\pm$  SEM).

(H) The A-V map with the markers of arterioles (arteriole 1: A1, arteriole 2: A2, red arrowheads) and optical fiber (green arrowhead).

(I) The seed-based correlation maps of CBV fMRI from one arterioles voxel (A1) overlaid on the A-V map.

(J) The correlation map between the CBV fMRI and calcium signal (band-pass filter: 0.01–0.1 Hz). Inset is a representative color-coded lag time map between the calcium signal and the CBV fMRI signal of individual arterioles ( $CC < -0.25$ ).

(K) The time course of the CBV fMRI signal from arteriole voxels (red, solid and dotted lines) and the slow oscillation calcium signal (green).

(L) The cross-correlation function of the calcium signal and CBV fMRI signal of two representative arterioles (Ca-A1 and Ca-A2) with negative peak coefficients at the lag time 1–2 s.

(M) The mean correlation coefficient of the calcium signal with the CBV fMRI signal of arterioles is significantly higher than that of venules ( $n = 4$ , mean  $\pm$  SEM, paired t test,  $***p = 0.0002$ ).

(N) The histogram of arterioles with lag times varied from 0.5 to 5 s ( $CC < -0.25$ ). The mean lag time is  $1.76 \pm 0.14$  s ( $n = 4$ , mean  $\pm$  SEM), which is significantly shorter than the lag times of the calcium and venule BOLD signal (BOLD,  $n = 7$ , CBV,  $n = 4$ , t test,  $p = 0.025$ ).

(O) The schematic drawing of the spatial and temporal correlation patterns of the slow oscillation signal coupling from neurons to vessels.

See also [Figures S4–S7](#) and [S10](#) and [Table S2](#)

Quantitative analysis showed that the correlation between the intracellular  $[Ca^{2+}]$  and the CBV-weighted signal of arterioles (Ca<sup>2+</sup>-A) was significantly higher than that of venules (Ca<sup>2+</sup>-V) (Figure 4M). The oscillation in intracellular  $[Ca^{2+}]$  also led the arteriole-specific CBV-weighted signal fluctuations, as observed by the cross-correlations of two representative arterioles as the function of lag time (Figure 4L). Different arterioles showed varied

lags with a mean value at  $1.8 \pm 0.2$  s (Figure 4N). Cross-correlation of the intracellular  $[Ca^{2+}]$  with the arteriole CBV-weighted signal showed a shorter lag time than that with the venule BOLD signal (Figures 4G and 4N). Meanwhile, the oscillation in intracellular  $[Ca^{2+}]$  was found to be correlated with the CBV-weighted signal of a few venules with lag time of 5–10 s (Figure S5). This result indicates the passive venule dilation usually

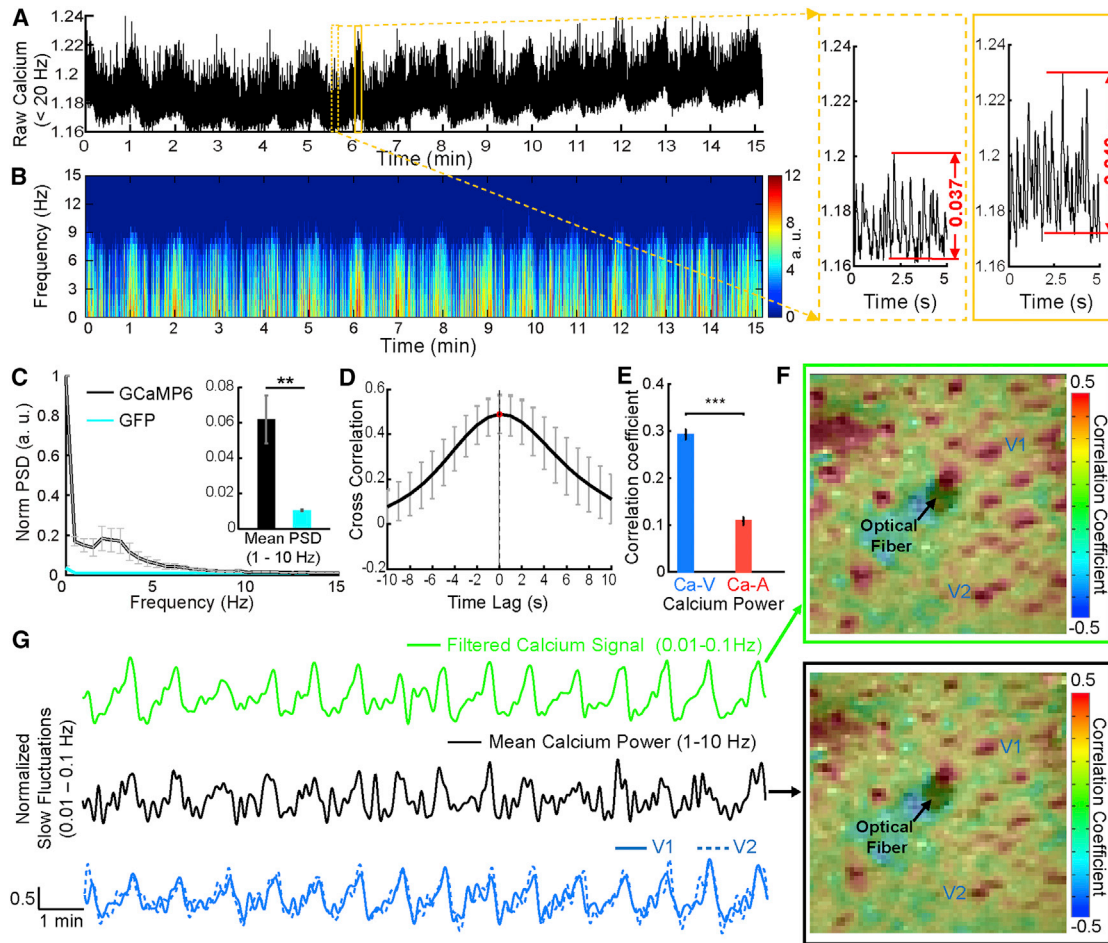


**Figure 5. The Correlation between the Calcium Power Spectral Profile with Vessel-Specific fMRI Signal**

(A) The time course of the calcium signal (low-pass filter: 20 Hz) from one representative rat at the resting state with enlarged 5 s windows of the calcium spikes identified at different periods (dotted and solid yellow boxes).

(B) The time-varying power spectrogram of the calcium signal is plotted as the function of time from 0.5 to 15 Hz (discrete Fourier transform in 1 s Hamming window; the sampling rate is 1 Hz to match the TR of fMRI signal).

(C) The normalized PSD from the rats with GCaMP6 (black,  $n = 5$ ) or GFP (cyan,  $n = 4$ ) indicates the mean PSD (1–10 Hz) of GCaMP6 is significantly higher than that of GFP (\*\* $p = 0.001$ ,  $t$  test).

(D) The cross-correlation function of the calcium signal and the averaged power (1–10 Hz) profile from the calcium spectrogram (band-pass filter with 0.01–0.1 Hz) illustrates the peak cross-correlation coefficient at 0 s lag time ( $n = 4$ , mean  $\pm$  SEM).

(E) The mean correlation coefficients of the averaged calcium power signal with the BOLD fMRI signal of venules are significantly higher than that of arterioles (\*\* $p = 1.9 \times 10^{-4}$ , pair  $t$  test,  $n = 4$ , mean  $\pm$  SEM).

(F) The correlation maps between the SSFP-based BOLD fMRI signal and the slow oscillation calcium signal (band-pass filter: 0.01–0.1 Hz, upper) and the mean calcium power spectral profile (1–10 Hz, lower) show similar venule-specific correlation patterns.

(G) The time series (band-pass filter: 0.01–0.1 Hz) of the slow oscillation calcium signal (green), the mean calcium spectral power profile (1–10 Hz) (black), the BOLD fMRI signal from two venules (V1, V2; blue, solid and dotted blue lines).

See also [Figure S6](#).

detected as the post-stimulus undershoot of the evoked BOLD signal results from increase blood flow following prolonged stimulation (Buxton et al., 1998; Silva et al., 2007; Drew et al., 2011).

Besides the ultra-slow oscillation, the GCaMP6-mediated calcium signal exhibited EEG-like rhythmic neuronal activity, showing significantly higher spectral power at the 1–10 Hz frequency range than that of the fluorescent signal detected from the GFP-expressing cortex of control rats (Figures 5A–5C). Cross-correlation of the spectral power in the 1–10 Hz and ul-

tra-slow oscillatory calcium signal fluctuation (0.1–0.01 Hz) showed peak positive correlation coefficient at zero time lag (Figure 5D). In addition, the spectral power in 1–10 Hz was correlated to the vessel-specific BOLD signal, showing the correlation coefficient of spectral power with the venule BOLD signal is significantly higher than that of the spectral power with the arteriole BOLD signal, similar to the ultra-slow oscillatory calcium signal fluctuation (Figures 4B–4D and 5E–5G). This result further demonstrates the neuronal correlates of the vessel-specific fMRI

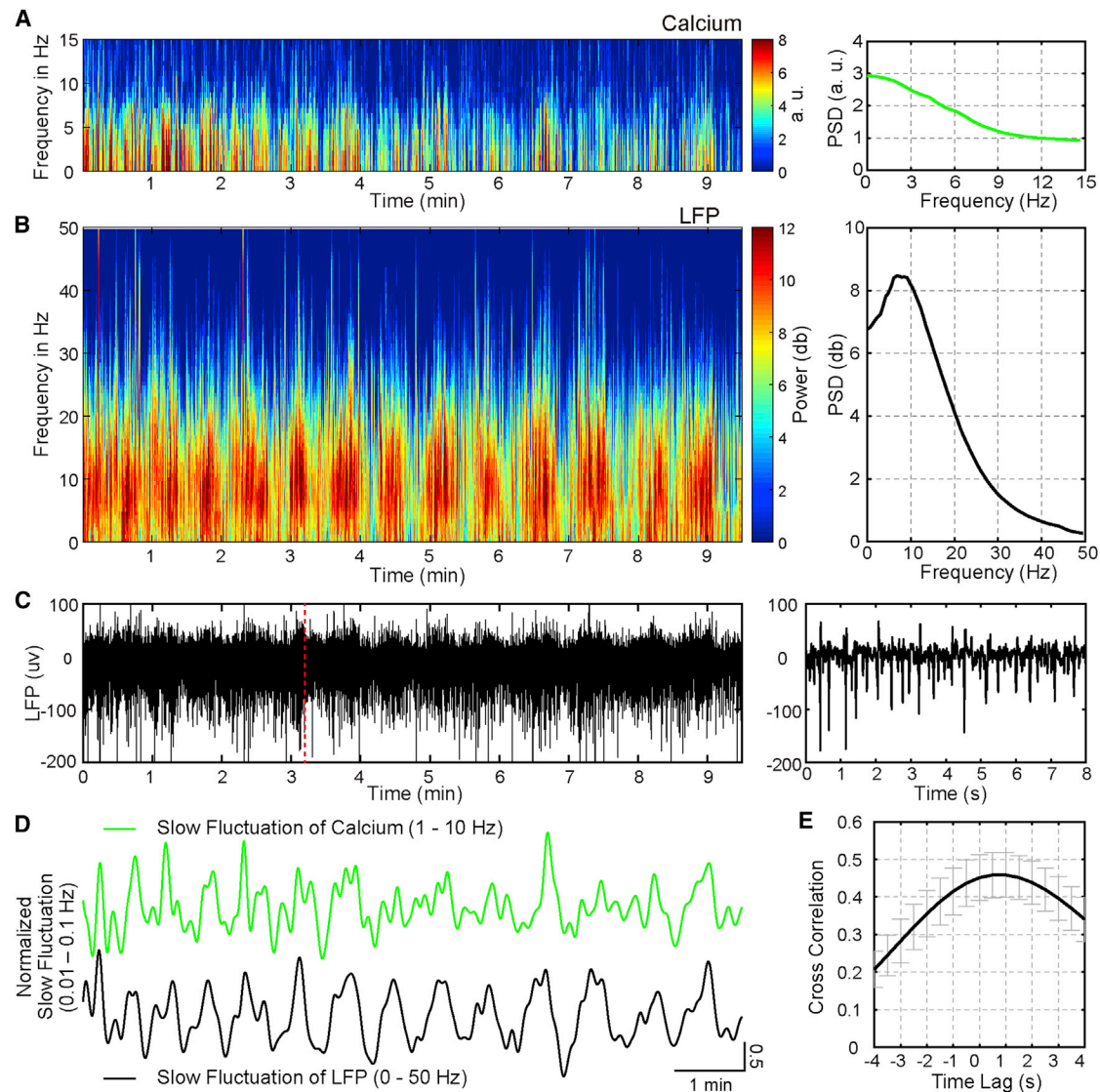


**Figure 6. The Spectrogram of Simultaneous Calcium and Electrophysiological Signal under  $\alpha$ -chloralose Anesthesia**

(A) Spectrogram of calcium signal during light anesthesia.  
 (B) Spectrogram of local field potential (LFP) at light anesthesia from multi-taper spectral estimates (1 s sliding window with 0.1 s steps, 9 tapers). The right panel shows the averaged power spectral density (PSD).  
 (C) The time course of the LFP signal under light anesthesia.  
 (D) The mean calcium spectral power profile (band-pass filter: 0.01–0.1 Hz of 1–10 Hz, green) and the mean LFP spectral power profile (0–50 Hz, black) at light anesthesia.  
 (E) The cross-correlation function of the averaged LFP power (0–50 Hz) from LFP spectrogram and the averaged calcium power (1–10 Hz) profile from the calcium spectrogram (band-pass filter with 0.01–0.1 Hz) illustrates the peak cross-correlation coefficient at 0.8 s lag time at light anesthesia ( $n = 4$ , mean  $\pm$  SEM). See also [Figures S5](#) and [S6](#).

signal fluctuation in the cerebrovascular network. Finally, the cartoon of [Figure 4O](#) summarizes the spatial and temporal patterns of neurovascular hemodynamic signal fluctuation from arteriolar to venous networks.

Also noteworthy is that the power spectral density shows elevated power at frequencies below 0.1 Hz for the venule BOLD and arteriole CBV-weighted signal, as well as for the simultaneously acquired calcium signal at the light anesthesia ([Figures 2D](#) and [S6](#)). In contrast, at the deep anesthesia level

with  $\alpha$ -chloralose, the ultra-slow oscillation pattern was undetectable for both fMRI and changes in  $[Ca^{2+}]$  concentration in the same rats ([Figure S6](#)), but the evoked BOLD and CBV fMRI signals and changes in  $[Ca^{2+}]$  concentration remained ([Figures S4E](#) and [S4F](#)). This result further supports the neural correlates of the single-vessel fMRI signal fluctuation. Meanwhile, simultaneous LFP and intracellular  $[Ca^{2+}]$  recording was performed to specify the ultra-slow oscillatory signal at different anesthesia levels ([Figures 6](#) and [S7](#)). The spectrogram of the spontaneous

LFP and intracellular  $[Ca^{2+}]$  signal showed similar ultra-slow oscillation patterns in rats under the light anesthesia level (Figures 6A–6D). Cross-correlation of the LFP and intracellular  $[Ca^{2+}]$  signal power profile showed positive correlation coefficients ( $0.46 \pm 0.06$ ) at the time lag ( $0.73 \pm 0.13$  s), showing the ultra-slow oscillatory LFP signal leads the intracellular  $[Ca^{2+}]$  signal (Figure 6E). Similar to the single-vessel fMRI data, these results showed consistent correlation features at the light anesthesia level (Figure 5) but not at the deep anesthesia (Figures S7A–S7E). In addition, the ultra-slow oscillatory correlation of the LFP power profile and intracellular  $[Ca^{2+}]$  fluctuations were detected in rats anesthetized with 1.2% (v/v) isoflurane (Figures S7F–S7I). These results suggest that the neuronal and vascular hemodynamic oscillations are highly correlated in the anesthetized brain and that the correlation is dampened when the neural activity is suppressed with deep anesthesia.

### Mapping Vascular Network Connectivity in the Human Brain under 3T and 9.4T

The single-vessel mapping scheme was implemented to characterize the prospects for vessel-specific fMRI correlation patterns in awake human subjects. Although bSSFP shows great advantage for the high-field fMRI in the rat brain as a consequence of decreased distortion and reduced extravascular effect compared to the EPI method, the single-echo bSSFP method acquires single k-space line per echo and takes longer time than the EPI method to acquire multi-slice high-resolution images (Budde et al., 2014). We established single-vessel fMRI human brain mapping with the EPI method. First, the fMRI signal of sulcus veins in the occipital lobe was mapped using EPI-fMRI at 3T. Upon the checkerboard visual stimulation, the evoked BOLD signal was located primarily at venous voxels with a sparsely distributed patchy pattern that was previously reported (Menon et al., 1993) (Figures 7A–7C and 7F; Movie S3). Besides the task-related functional maps, the seed-based correlation maps from resting-state fMRI demonstrated vein-dominated correlation spatial patterns (Figures 7D and 7G; Movie S4). The coherence analysis of paired venous voxels showed coherent ultra-slow oscillation of the awake human subjects up to  $\sim 0.1$  Hz (Figure 7H), which was much higher than the oscillation frequency detected in anesthetized rats (Figure 3H). The correlation coefficients of paired venous voxels were plotted as the function of the intra-hemispheric and inter-hemispheric vessel distances (Figure 7I). The values of the correlation decreased as the function of the intra-hemispheric vessel distance but showed significantly higher values for the inter-hemispheric venous voxel pairs (Figure 7J), similar to previously established spatial vasomotion correlation patterns in awake mice (Mateo et al., 2017). The low-frequency oscillation around 0.1 Hz has been previously reported in the visual cortex of the human brain with conventional resting-state fMRI method (Mittra et al., 1997). Also, when EPI images were spatially smoothed with different kernels from 1 to 5 mm, the vessel-specific spatial patterns merged to functional blobs similar to the conventional functional connectivity maps (Biswal et al., 1995; Smith et al., 2009) (Figures 7K and 7L).

The seed-based analysis was performed before and after the regression of respiration and heartbeat relevant temporal artifacts (Figures S8A–S8F), showing the little difference in the

vessel-specific spatial patterns (Figures S8G–S8M). In addition, ICA analysis specified the highly correlated venous voxels at multiple slices, showing a 3D vascular dynamic correlation structure through the main branches of cerebral vasculature (Figures S9A–S9D; Movie S5). These results demonstrate that the hemodynamic fMRI signals from central veins through sulci or at the gyrus surface are highly correlated, representing large-scale vascular dynamic network connectivity detectable with the 3T MR scanner.

To characterize the hemodynamic signal fluctuation in vessels penetrating cortical gray matter, we mapped the single vessel-based resting-state fMRI signal at 9.4T. The multiple 2D EPI images were acquired with an in-plane resolution of  $500 \times 500 \mu\text{m}^2$  and  $800 \mu\text{m}$  thickness at a TR of 1 s. In parallel, a single-vessel A-V map was acquired to better characterize the location of individual sulcus arteries and veins, as well as a few intracortical veins (Figures 8A–8C). Similarly, the BOLD signal was highly correlated on venous voxels, but not on artery voxels (Figures 8D and 8E). In the enlarged correlation maps, a few intracortical veins penetrating the gray matter could be spotted on the A-V map, given their unique vascular orientation through the 2D slice, showing a strong correlation to each other (Figures 8B, 8C, S9E, and S9F). Furthermore, coherence analysis of paired veins showed a coherent frequency range less than  $\sim 0.1$  Hz, which is consistent with previous brain ultra-slow oscillation studies (Obrig et al., 2000) (Figure 8G). This result provides a good example for the illustration of vascular correlation of the selected intracortical veins penetrating cortical gray matter at 9.4T. This result shows the translational potential of high-resolution single-vessel fMRI to associate anatomical vascular biomarkers with prognostic dynamic indicators of neurovascular disease and vascular dementia in the brain.

## DISCUSSION

We have demonstrated that a single-vessel fMRI mapping scheme reveals the spatial and temporal features of vessel-to-vessel hemodynamic correlations in anesthetized rats and in awake human subjects. With regard to rats, BOLD-specific venous signals and the CBV-specific arteriolar signals evolve at ultra-slow timescales, with frequency components between 0.01 and 0.04 Hz (Figure 3). Both signals show a causal relationship to the simultaneously acquired calcium signal (Figure 4). With regard to humans, the ultra-slow oscillation was observed in the BOLD signal for frequencies up to 0.1 Hz and vessel-to-vessel correlations are strong (Figure 8). This work demonstrates the feasibility to apply a multi-modal fMRI platform to measure the neuronal correlates of resting-state hemodynamic signal fluctuation from arteriolar to venous networks at the scale of individual vessels.

### Technical Advances

The attainment of single-vessel imaging with high SNR was achieved based on three factors: a high magnetic field to enhance the transverse signal; a bSSFP sequence with high SNR efficiency per time unit; and a small radio frequency coil with appropriate sample loading to optimize the detection from local cortical regions. These factors ensured that the temporal

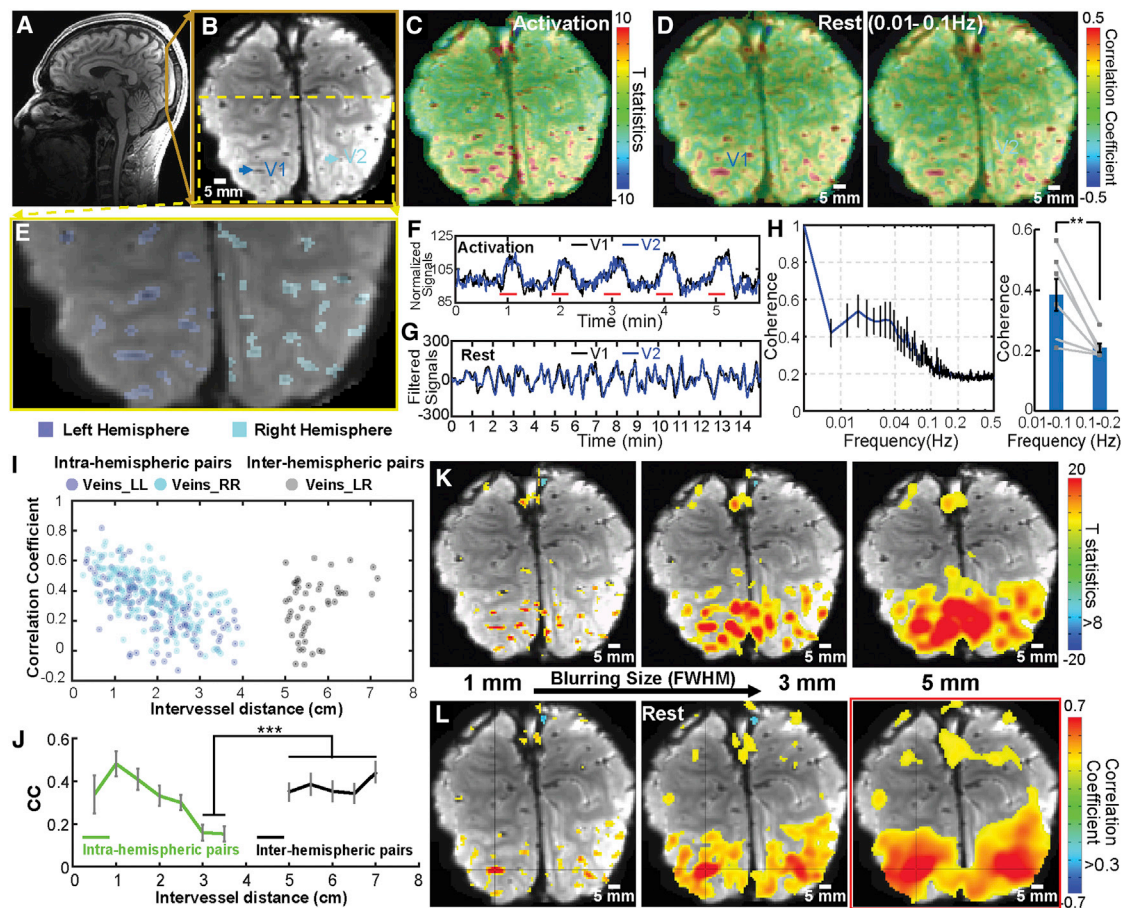


**Figure 7. The Task-Related and Resting-State Single-Vessel fMRI Mapping in Awake Human Subjects at 3T**

(A) A sagittal view of the human brain with a 2D EPI slice located in the occipital lobe.  
 (B) An averaged EPI image shows the pial veins in sulci as dark dots.  
 (C) The checkerboard visual stimulation-evoked BOLD functional map with peak BOLD signals located at pial veins.  
 (D) The seed-based BOLD correlation maps (0.01–0.1 Hz; seeds: two veins [V1 and V2]) demonstrate vessel-dominated patterns.  
 (E) The magnified view of the averaged EPI image from one representative subject (vein ROIs, left hemisphere, blue, right hemisphere, cyan).  
 (F and G) The time courses of two veins in the task-related (F) and resting-state (G) (0.01–0.1 Hz) conditions.  
 (H) The coherence graph of paired veins exhibits coherent oscillation at the frequency range of 0.01–0.1 Hz significantly higher than the higher frequency range (0.1–0.2 Hz;  $n = 6$ , mean  $\pm$  SEM, \*\*, paired  $t$  test,  $p = 0.008$ ).  
 (I) The scatterplot of the correlation coefficient (CC) from intra and inter-hemispheric vein pairs.  
 (J) The mean CC of inter-hemispheric vein pairs with the intervessel distance between 5–7 cm is significantly higher than that of intra-hemispheric vein pairs with distance between 3–3.5 cm. (\*\*\*,  $n = 6$ , mean  $\pm$  SEM,  $t$  test,  $p = 0.0002$ ).  
 (K and L) The evoked functional (K) and resting-state correlation (L) maps were smoothed from 1 mm to 5 mm (FWHM).  
 See also [Figures S8](#) and [S9](#).

fluctuation of the vessel-specific fMRI signal was not dominated by machine-based technical noise, but rather represented the physiological state of the brain. This issue was further verified by the anesthetic dose-dependent study, which indicated that the vessel-specific fMRI signal fluctuation could be dampened even though the SNR remained unchanged ([Figure S6](#)). Besides the technical noise, artifacts from physiological motion can be erroneously intrinsically linked to the functional connectivity ([Hu et al., 1995; Murphy et al., 2013](#)). Numerous strategies have been developed to regress out the potential artifacts, or identify the functional node-specific component using ICA analysis ([Glover et al., 2000; McKeown et al., 2003](#)). Nonetheless, a

lack of standard criteria to distinguish the contribution from brain signal fluctuation versus physiological motion artifacts limits the reliability of functional connectivity. We nominally expect that the pattern of correlations should be insensitive to global motion artifacts. Further, the enhanced correlations in the BOLD response for pairs of venules versus arterioles ([Figures 3F, 3H, 3J, and 8F](#)) and the enhanced correlations in the CBV response for arterioles versus venules ([Figures 3G, 3I, and K](#)) as a function of frequency are highly unlikely to result from known artifacts.

The detected bSSFP signal change is a mixture of intravascular and extravascular contributions. The intravascular signal is given by the steady-state contrast of passband bSSFP, which

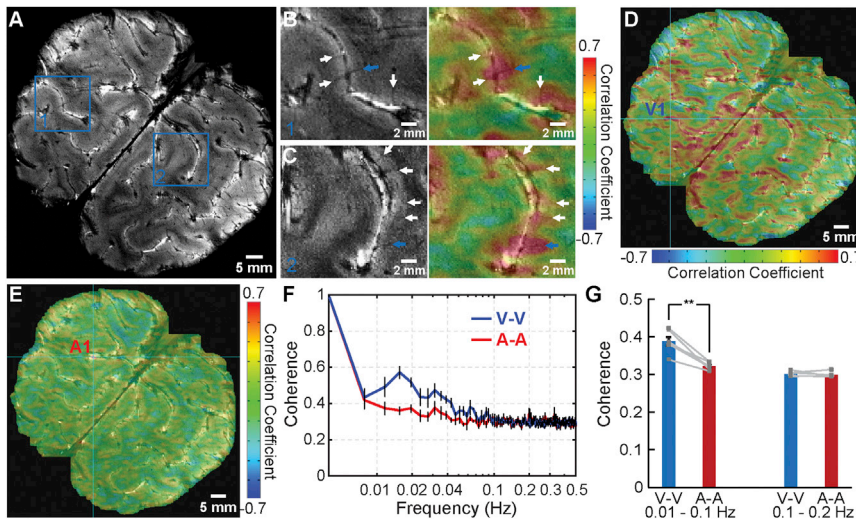


**Figure 8. The Intracortical Vascular Dynamic Mapping with 9.4T**

(A) The A-V map is acquired from a 2D slice across the occipital lobe. (B and C) The intra-cortical veins (arrows) in the magnified view of region 1 and region 2 in the A-V map (left). The right panel shows the correlation map based on the selected seeds (the intra-cortical veins: blue arrows) with highly correlated voxels detected on the other intracortical veins (white arrows) in the gray matter. (D and E) The seed-based correlation maps with vein 1 (V1), artery 1 (A1) as seeds, respectively (seeds: cyan crosshairs). (F) The coherence graph of paired veins (blue) and arteries (red) identified by the AV map demonstrates the slow fluctuations from 0.01 to 0.1 Hz. (G) The mean coherence coefficients of the paired veins are significantly higher than that of the paired arteries at low frequency (0.01–0.1 Hz) ( $n = 6$ , mean  $\pm$  SEM, paired t test,  $**p = 0.0009$ ). See also Figure S9.

is proportional to  $\sqrt{T_2/T_1}$  (Scheffler and Lehnardt, 2003). Given the high spatial resolution of the bSSFP fMRI imaging, the BOLD contrast from venules and the CBV-based contrast from arterioles of vessel voxels remained highly T2-weighted because of the fast T2 decay of deoxygenated venule blood and iron oxide enriched arteriole blood (Lee et al., 1999; Blockley et al., 2008). The extravascular contribution depends on the vessel size. As for spin echoes, the rapid refocusing in bSSFP produces dynamic averaging that reduces the extravascular effects of the cortical penetrating vessels larger than 10–20  $\mu\text{m}$  (Bieri and Scheffler, 2007; Scheffler and Ehse, 2016). Therefore, the observed signal changes with high spatial resolution bSSFP were mainly intravascular. It is noteworthy that the blood flow could contribute to the BOLD fMRI signal fluctuation based on the in-flow effect, given the short TR of the bSSFP sequence at a given flip angle (Kim et al., 1994). This is especially true for arterioles. However, the BOLD signal fluctuation in arterioles showed significantly lower correlation than that of venules, indicating that the in-flow effect is not the primary contributor to the vascular dynamic correlation patterns (Figures 2 and 3).

### BOLD versus CBV-Weighted fMRI Signals

In contrast to the venous BOLD signal, for the CBV signal fluctuation, the arteriole-dominated CBV-signal results from vasomotor fluctuations in vessel diameter. The vasomotion signal shows ultra-slow oscillation with a broader frequency band centered at 0.1 Hz in the anesthetized rat brain (Mayhew et al., 1996; Kleinfeld et al., 1998) and 0.1 Hz in awake mice (Drew et al., 2010). Although in the present study arteriole CBV signal fluctuations were detected at a frequency band of  $<0.04$  Hz in  $\alpha$ -chloralose anesthetized rats, it is likely that this hemodynamic signal corresponds to vasomotion. Further to this point, beyond the neuronal effects of anesthetics (Brown et al., 2011; Mateo et al., 2017), anesthetics may directly affect vasomotion and directly contribute to the temporal dynamic patterns detected by fMRI in anesthetized animals (Colantuoni et al., 1984; Hundley et al., 1988). In addition, future studies will compare the arteriole-

specific fMRI signal fluctuation in rat under anesthesia and wakefulness to specify the dynamic patterns driven by vasomotion. Lastly, our result is also consistent with the “bagpipe” model of active arteriole dilation with increased neuronal activity, where arteriole dynamics dominate both spontaneous and evoked blood volume changes in the brain (Drew et al., 2011). Following the net increase of the arteriole blood reservoir, venules drain the blood with a delayed passive dilation, which is consistent with undershoot of the evoked BOLD fMRI signal (Mandeville et al., 1999).

The ultra-slow passive venule dilation was detected by single-vessel CBV-bSSFP fMRI when iron oxide particles were delivered at a lower than normal dosage so that the venule fMRI signal was not completely dampened due to shortened  $T_2^*$  decay (Figure S5). This observation also explains the small number of venules highlighted by the arteriole-seed-based CBV correlation maps (Figure 2C), which showed much longer lag time than arterioles when analyzing the simultaneously acquired calcium ultra-slow oscillation signal via cross-correlation (Figure S5). All told, single-vessel bSSFP-fMRI detects distinct spatial and temporal patterns of vessel-specific dynamic connectivity in the anesthetized rat brain.

### Correlates of Neuronal $[\text{Ca}^{2+}]$ and Single-Vessel fMRI

A key observation was the correlation of ultra-slow calcium oscillation with single-vessel fMRI signal fluctuation. Prior combined fMRI and electrophysiological studies show that the resting-state BOLD signal correlates with neuronal activity oscillation (He et al., 2008; Shmuel and Leopold, 2008; Schölvinc et al., 2010; Pan et al., 2013). The present study extends the spatial resolution of resting-state fMRI down to single vessels. The coherence of the ultra-slow oscillations from both intracellular  $[\text{Ca}^{2+}]$  and vessel-specific fMRI signals demonstrates a potential link of the two events, with the calcium event leading the vascular fluctuation (Figures 4E and 4L). In particular, the BOLD signal from individual venules and the CBV-weighted signal detected primarily from arterioles showed

varied lag times, ranging from 0.5 to 6 s, relative to the calcium signal (Figures 4G and 4N).

Previous studies reported only long, i.e., 5 to 6 s, lag times by cross-correlation of the change in  $\gamma$ -band power and the resting-state BOLD signal (Schölvinck et al., 2010). This long lag time could be caused by signal fluctuations in large voxels, with primary weighting on surface draining veins. In the present study, the fMRI signal from draining veins also showed longer lag time, which is consistent with the lag time between the calcium and hemoglobin signal oscillation ( $\sim 0.1$  Hz) detected from the cortical surface (Du et al., 2014). In contrast to surface draining veins, penetrating vessels at the deep cortical layers showed shorter lag times of  $1.8 \pm 0.2$  s for the arteriole CBV signal and  $2.3 \pm 0.2$  s for the venule BOLD signal (Figure 4), which is in concordance with the signaling order of arteriole dilation followed by oxygen saturation changes in venules for neurovascular coupling (Devor et al., 2003; Iadecola, 2004).

The arterio-venous (A-V) transit time of the resting-state hemodynamic signal was calculated based on the cross-correlation lag times of the BOLD and CBV-weighted signals to the simultaneously recorded calcium signal (Figure S10 and Table S2). The resting-state A-V transit time of 0.61 s at the deep cortical layers is slightly shorter than the transit time of 0.8–1.2 s, calculated by the time to half-maximal,  $t_{1/2}$ , from surface arterioles to venules (Hutchinson et al., 2006). This further supports the vessel-specific hemodynamic signal propagation. Also noteworthy is that the variability of the measured resting-state transit time is relatively higher than that of the evoked A-V hemodynamic transit time (Yu et al., 2016) (Figure S10), indicating a more heterogeneous hemodynamic coupling during the resting state. Lastly, cortical calcium waves have been observed in the newborn and adult rodent brain (Adelsberger et al., 2005; Ma et al., 2016) and can propagate through the cortex at a fast speed (Stroh et al., 2013). It will be interesting to determine whether these drive propagating vascular events.

### Single-Vessel Human Maps

Vascular dynamic network connectivity was directly mapped in awake human subjects to demonstrate the translational potential of single-vessel fMRI mapping. The vessel-specific ultra-slow oscillation shares a similar frequency range to that of the long-distance functional nodes detected by conventional resting-state fMRI, as well as the spontaneous oscillation of the cerebral hemodynamic signal detected by near-infrared spectroscopy (Obrig et al., 2000). In addition, the smoothed single-vessel correlation maps represented similar functional connectivity maps in the visual area as detected by the conventional resting-state fMRI (Smith et al., 2009) (Figures 7K and 7L). Together with the rat data that show highly correlated calcium and single-vessel fMRI signal fluctuation, the vascular dynamic network connectivity could represent the hemodynamic vascular correlation coupled to neuronal signal oscillation in both anesthetized and awake conditions. Interestingly, a recent resting-state fMRI study showed that the connectivity strength of a given voxel among the “default mode” and other networks is inversely proportional to its vascular volume fraction (Tak et al., 2015). This observation indicates that functional connectivity of long-range

nodes in the brain may be driven independently of the vascular-specific hemodynamic fluctuation. Given the highly correlated calcium signal to the hemodynamic signal fluctuation, one possible explanation for this discrepancy is that vascular dynamic network connectivity represents the whole brain state fluctuation with less region specificity (Chang et al., 2016), but the functional connectivity may specify the network pattern of long-distance functional nodes (Biswal et al., 1995; Smith et al., 2009). Alternatively, because the vascular volume fraction was calculated from the largest extracerebral vessels detected by MRI images, it is also possible that the reduced connectivity may be caused by the low SNR of voxels occupied by these extracerebral vessels.

Given the cerebral folds and fissures of the human brain, single-vessel EPI-fMRI mapping mainly detects the central pial veins through the sulci with diameters of a few hundred micrometers based on the T2\*-weighted partial volume effect. Single-vessel fMRI with 9.4T at high spatial resolution, i.e.,  $500 \times 500 \times 800 \mu\text{m}^3$ , showed the correlation patterns of the intracortical penetrating veins in the human brain (Duvernoy et al., 1981) (Figure 8). In contrast to studies focusing on excluding the venous BOLD signal to improve spatial specificity for brain function and connectivity mapping (Barth and Norris, 2007; Curtis et al., 2014), this work specifies the vascular network connectivity in gray matter of the human brain with the potential clinical application of illustrating hemodynamic features of vascular dementia (O'Brien et al., 2003; Iadecola, 2013). Specifically, the neural correlates of the vascular dynamic network connectivity detected in the rodent brain display great potential for clinical applications such as the diagnosis of cognitive impairments in patients with cerebral small vessel diseases or degenerative diseases such as Alzheimer's disease (Schaefer et al., 2014). The ability to specify the direct linkage of vascular pathology to dysfunction of the neurovascular network remains elusive (Stevens et al., 2014). The ability to map the hemodynamic origin of the BOLD signal from anatomically distinguishable vessels in human gray matter provides a key step to link vascular biomarkers, e.g., microbleeds (Poels et al., 2012) or cortical microinfarcts (van Veluw et al., 2013; van Rooden et al., 2014), with dynamic indicators in patients with small vessel or Alzheimer's disease.

### Caveats Going Forward

We developed the single-vessel fMRI resting-state mapping scheme to characterize the spatial and temporal hemodynamic signals in arteriolar and venous networks, concurrent with photometric calcium recording. The high field MRI scanner, 14T for animals and 9.4T for humans, achieves sufficient SNR and high BOLD contrast for high-resolution fMRI imaging. A redesign of the radio frequency detection coil will be needed to extend the single-vessel fMRI method to broader application with lower magnetic field scanners. Toward this goal, a super-conducting coil has been developed to boost the SNR of MRI images (Ratering et al., 2008). Also, instead of the current 32- or 64-channel coils for human brain imaging, region-specific array coils can be developed to cover focal cortical areas with optimized geometry to increase the SNR. This step will help further resolve individual intracortical vessels in gray matter of normal human

subjects as well as patients with neurovascular dysfunction due to vascular dementia.

## STAR★METHODS

Detailed methods are provided in the online version of this paper and include the following:

- [KEY RESOURCES TABLE](#)
- [CONTACT FOR REAGENT AND RESOURCE SHARING](#)
- [EXPERIMENTAL MODELS AND SUBJECT DETAILS](#)
  - Animals
  - Human Subjects
- [METHODS DETAILS](#)
  - Animal experiments
  - MRI image acquisition from rats (14.1T)
  - MRI image acquisition from humans (3 T)
  - MRI image acquisition from humans (9.4 T)
  - Data processing
  - Immunohistochemistry
- [QUANTIFICATION AND STATISTICAL ANALYSIS](#)

## SUPPLEMENTAL INFORMATION

Supplemental Information includes ten figures, three tables, and five movies and can be found with this article online at <https://doi.org/10.1016/j.neuron.2018.01.025>.

## ACKNOWLEDGMENTS

This research was supported by Germany Research Foundation (DFG) SPP-1655 and internal funding from Max Planck Society for X.Y. and NIH grants R35NS097265 for D.K. and NIMH BRAIN grant R01MH11438 for D.K. and B.R.R. We thank Dr. H. Merkle and Dr. K. Buckenmaier for technical support, Ms. H. Schulz and Ms. S. Fischer for animal maintenance support, the AFNI team for the software support, and Dr. L. Looger and the Janelia Research Campus of HHMI for kindly providing viral vectors.

## AUTHOR CONTRIBUTIONS

X.Y., D.K., and B.R.R. designed the research, Y.H., X.Y., M.W., and X.C. performed animal experiments, Y.H., X.Y., and R.P. acquired data, X.Y. supervised the research, Y.H. analyzed data, K.S., R.P., J.R.P., and M.W. provided key technical support, and X.Y., D.K., and Y.H. wrote the manuscript.

## DECLARATION OF INTERESTS

The authors declare no competing interests.

Received: June 26, 2017

Revised: November 14, 2017

Accepted: January 10, 2018

Published: February 1, 2018

## REFERENCES

Adelsberger, H., Garaschuk, O., and Konnerth, A. (2005). Cortical calcium waves in resting newborn mice. *Nat. Neurosci.* *8*, 988–990.

Aydin, F., Rosenblum, W.I., and Povlishock, J.T. (1991). Myoendothelial junctions in human brain arterioles. *Stroke* *22*, 1592–1597.

Barth, M., and Norris, D.G. (2007). Very high-resolution three-dimensional functional MRI of the human visual cortex with elimination of large venous vessels. *NMR Biomed.* *20*, 477–484.

Bell, A.J., and Sejnowski, T.J. (1995). An information-maximization approach to blind separation and blind deconvolution. *Neural Comput.* *7*, 1129–1159.

Bieri, O., and Scheffler, K. (2007). Effect of diffusion in inhomogeneous magnetic fields on balanced steady-state free precession. *NMR Biomed.* *20*, 1–10.

Biswal, B., Yetkin, F.Z., Haughton, V.M., and Hyde, J.S. (1995). Functional connectivity in the motor cortex of resting human brain using echo-planar MRI. *Magn. Reson. Med.* *34*, 537–541.

Blinder, P., Tsai, P.S., Kaufhold, J.P., Knutsen, P.M., Suhl, H., and Kleinfeld, D. (2013). The cortical angiome: an interconnected vascular network with noncolumnar patterns of blood flow. *Nat. Neurosci.* *16*, 889–897.

Blockley, N.P., Jiang, L., Gardener, A.G., Ludman, C.N., Francis, S.T., and Gowland, P.A. (2008). Field strength dependence of R1 and R2\* relaxivities of human whole blood to ProHance, Vasovist, and deoxyhemoglobin. *Magn. Reson. Med.* *60*, 1313–1320.

Brown, E.N., Purdon, P.L., and Van Dort, C.J. (2011). General anesthesia and altered states of arousal: a systems neuroscience analysis. *Annu. Rev. Neurosci.* *34*, 601–628.

Budde, J., Shajan, G., Zaitsev, M., Scheffler, K., and Pohmann, R. (2014). Functional MRI in human subjects with gradient-echo and spin-echo EPI at 9.4 T. *Magn. Reson. Med.* *71*, 209–218.

Buxton, R.B., Wong, E.C., and Frank, L.R. (1998). Dynamics of blood flow and oxygenation changes during brain activation: the balloon model. *Magn. Reson. Med.* *39*, 855–864.

Chan, A.W., Mohajerani, M.H., LeDue, J.M., Wang, Y.T., and Murphy, T.H. (2015). Mesoscale infraslow spontaneous membrane potential fluctuations recapitulate high-frequency activity cortical motifs. *Nat. Commun.* *6*, 7738.

Chang, C., Leopold, D.A., Schölvinc, M.L., Mandelkow, H., Picchioni, D., Liu, X., Ye, F.Q., Turchi, J.N., and Duyn, J.H. (2016). Tracking brain arousal fluctuations with fMRI. *Proc. Natl. Acad. Sci. USA* *113*, 4518–4523.

Chen, T.W., Wardill, T.J., Sun, Y., Pulver, S.R., Renninger, S.L., Baohan, A., Schreiter, E.R., Kerr, R.A., Orger, M.B., Jayaraman, V., et al. (2013). Ultrasensitive fluorescent proteins for imaging neuronal activity. *Nature* *499*, 295–300.

Colantuoni, A., Bertuglia, S., and Intaglietta, M. (1984). Effects of anesthesia on the spontaneous activity of the microvasculature. *Int. J. Microcirc. Clin. Exp.* *3*, 13–28.

Cox, R.W. (1996). AFNI: software for analysis and visualization of functional magnetic resonance neuroimages. *Comput. Biomed. Res.* *29*, 162–173.

Curtis, A.T., Hutchison, R.M., and Menon, R.S. (2014). Phase based venous suppression in resting-state BOLD GE-fMRI. *Neuroimage* *100*, 51–59.

Delorme, A., and Makeig, S. (2004). EEGLAB: an open source toolbox for analysis of single-trial EEG dynamics including independent component analysis. *J. Neurosci. Methods* *134*, 9–21.

Devor, A., Dunn, A.K., Andermann, M.L., Ulbert, I., Boas, D.A., and Dale, A.M. (2003). Coupling of total hemoglobin concentration, oxygenation, and neural activity in rat somatosensory cortex. *Neuron* *39*, 353–359.

Drew, P.J., Duyn, J.H., Golanov, E., and Kleinfeld, D. (2008). Finding coherence in spontaneous oscillations. *Nat. Neurosci.* *11*, 991–993.

Drew, P.J., Shih, A.Y., Driscoll, J.D., Knutsen, P.M., Blinder, P., Davalos, D., Akassoglou, K., Tsai, P.S., and Kleinfeld, D. (2010). Chronic optical access through a polished and reinforced thinned skull. *Nat. Methods* *7*, 981–984.

Drew, P.J., Shih, A.Y., and Kleinfeld, D. (2011). Fluctuating and sensory-induced vasodynamics in rodent cortex extend arteriole capacity. *Proc. Natl. Acad. Sci. USA* *108*, 8473–8478.

Du, C., Volkow, N.D., Koretsky, A.P., and Pan, Y. (2014). Low-frequency calcium oscillations accompany deoxyhemoglobin oscillations in rat somatosensory cortex. *Proc. Natl. Acad. Sci. USA* *111*, E4677–E4686.

Duvernoy, H.M., Delon, S., and Vannson, J.L. (1981). Cortical blood vessels of the human brain. *Brain Res. Bull.* *7*, 519–579.

Fox, M.D., and Raichle, M.E. (2007). Spontaneous fluctuations in brain activity observed with functional magnetic resonance imaging. *Nat. Rev. Neurosci.* *8*, 700–711.

- Glover, G.H., Li, T.Q., and Ress, D. (2000). Image-based method for retrospective correction of physiological motion effects in fMRI: RETROICOR. *Magn. Reson. Med.* 44, 162–167.
- He, B.J., Snyder, A.Z., Zempel, J.M., Smyth, M.D., and Raichle, M.E. (2008). Electrophysiological correlates of the brain's intrinsic large-scale functional architecture. *Proc. Natl. Acad. Sci. USA* 105, 16039–16044.
- Hirsch, S., Reichold, J., Schneider, M., Székely, G., and Weber, B. (2012). Topology and hemodynamics of the cortical cerebrovascular system. *J. Cereb. Blood Flow Metab.* 32, 952–967.
- Hu, X., Le, T.H., Parrish, T., and Erhard, P. (1995). Retrospective estimation and correction of physiological fluctuation in functional MRI. *Magn. Reson. Med.* 34, 201–212.
- Hundley, W.G., Renaldo, G.J., Levasseur, J.E., and Kontos, H.A. (1988). Vasomotion in cerebral microcirculation of awake rabbits. *Am. J. Physiol.* 254, H67–H71.
- Hutchinson, E.B., Stefanovic, B., Koretsky, A.P., and Silva, A.C. (2006). Spatial flow-volume dissociation of the cerebral microcirculatory response to mild hypercapnia. *Neuroimage* 32, 520–530.
- Iadecola, C. (2004). Neurovascular regulation in the normal brain and in Alzheimer's disease. *Nat. Rev. Neurosci.* 5, 347–360.
- Iadecola, C. (2013). The pathobiology of vascular dementia. *Neuron* 80, 844–866.
- Intaglietta, M. (1990). Vasomotion and flowmotion: physiological mechanisms and clinical evidence. *Vasc. Med. Rev.* 1, 101–112.
- Kim, S.G., Hendrich, K., Hu, X., Merkle, H., and Ugurbil, K. (1994). Potential pitfalls of functional MRI using conventional gradient-recalled echo techniques. *NMR Biomed.* 7, 69–74.
- Kleinfeld, D., Mitra, P.P., Helmchen, F., and Denk, W. (1998). Fluctuations and stimulus-induced changes in blood flow observed in individual capillaries in layers 2 through 4 of rat neocortex. *Proc. Natl. Acad. Sci. USA* 95, 15741–15746.
- Lee, S.P., Silva, A.C., Ugurbil, K., and Kim, S.G. (1999). Diffusion-weighted spin-echo fMRI at 9.4 T: microvascular/tissue contribution to BOLD signal changes. *Magn. Reson. Med.* 42, 919–928.
- Logothetis, N.K., Pauls, J., Augath, M., Trinath, T., and Oeltermann, A. (2001). Neurophysiological investigation of the basis of the fMRI signal. *Nature* 412, 150–157.
- Longden, T.A., Dabertrand, F., Koide, M., Gonzales, A.L., Tykocki, N.R., Brayden, J.E., Hill-Eubanks, D., and Nelson, M.T. (2017). Capillary K<sup>+</sup>-sensing initiates retrograde hyperpolarization to increase local cerebral blood flow. *Nat. Neurosci.* 20, 717–726.
- Ma, Y., Shaik, M.A., Kozberg, M.G., Kim, S.H., Portes, J.P., Timerman, D., and Hillman, E.M. (2016). Resting-state hemodynamics are spatiotemporally coupled to synchronized and symmetric neural activity in excitatory neurons. *Proc. Natl. Acad. Sci. USA* 113, E8463–E8471.
- Mandeville, J.B., Marota, J.J., Kosofsky, B.E., Keltner, J.R., Weissleder, R., Rosen, B.R., and Weisskoff, R.M. (1998). Dynamic functional imaging of relative cerebral blood volume during rat forepaw stimulation. *Magn. Reson. Med.* 39, 615–624.
- Mandeville, J.B., Marota, J.J., Ayata, C., Zaharchuk, G., Moskowitz, M.A., Rosen, B.R., and Weisskoff, R.M. (1999). Evidence of a cerebrovascular post-arteriole windkessel with delayed compliance. *J. Cereb. Blood Flow Metab.* 19, 679–689.
- Mansfield, P., Maudsley, A.A., and Baines, T. (1976). Fast Scan Proton Density Imaging by Nmr. *J. Phys. E Sci. Instrum.* 9, 271–278.
- Mateo, C., Knutsen, P.M., Tsai, P.S., Shih, A.Y., and Kleinfeld, D. (2017). Entrainment of arteriole vasomotor fluctuations by neural activity is a basis of blood-oxygenation-level-dependent “resting-state” connectivity. *Neuron* 96, 936–948.e3.
- Mayhew, J.E., Askew, S., Zheng, Y., Porrill, J., Westby, G.W., Redgrave, P., Rector, D.M., and Harper, R.M. (1996). Cerebral vasomotion: a 0.1-Hz oscillation in reflected light imaging of neural activity. *Neuroimage* 4, 183–193.
- McKeown, M.J., Hansen, L.K., and Sejnowski, T.J. (2003). Independent component analysis of functional MRI: what is signal and what is noise? *Curr. Opin. Neurobiol.* 13, 620–629.
- Menon, R.S., Ogawa, S., Tank, D.W., and Ugurbil, K. (1993). Tesla gradient recalled echo characteristics of photic stimulation-induced signal changes in the human primary visual cortex. *Magn. Reson. Med.* 30, 380–386.
- Mitra, P.P., Ogawa, S., Hu, X., and Ugurbil, K. (1997). The nature of spatiotemporal changes in cerebral hemodynamics as manifested in functional magnetic resonance imaging. *Magn. Reson. Med.* 37, 511–518.
- Moon, C.H., Fukuda, M., and Kim, S.G. (2013). Spatiotemporal characteristics and vascular sources of neural-specific and -nonspecific fMRI signals at submillimeter columnar resolution. *Neuroimage* 64, 91–103.
- Murphy, K., Birn, R.M., and Bandettini, P.A. (2013). Resting-state fMRI confounds and cleanup. *Neuroimage* 80, 349–359.
- O'Brien, J.T., Erkinjuntti, T., Reisberg, B., Roman, G., Sawada, T., Pantoni, L., Bowler, J.V., Ballard, C., DeCarli, C., Gorelick, P.B., et al. (2003). Vascular cognitive impairment. *Lancet Neurol.* 2, 89–98.
- Obrig, H., Neufang, M., Wenzel, R., Kohl, M., Steinbrink, J., Einhüpl, K., and Villringer, A. (2000). Spontaneous low frequency oscillations of cerebral hemodynamics and metabolism in human adults. *Neuroimage* 12, 623–639.
- Pan, W.J., Thompson, G.J., Magnuson, M.E., Jaeger, D., and Keilholz, S. (2013). Infraslow LFP correlates to resting-state fMRI BOLD signals. *Neuroimage* 74, 288–297.
- Poels, M.M., Ikram, M.A., van der Lugt, A., Hofman, A., Niessen, W.J., Krestin, G.P., Breteler, M.M., and Vernooij, M.W. (2012). Cerebral microbleeds are associated with worse cognitive function: the Rotterdam Scan Study. *Neurology* 78, 326–333.
- Poplawsky, A.J., Fukuda, M., Kang, B.M., Kim, J.H., Suh, M., and Kim, S.G. (2017). Dominance of layer-specific microvessel dilation in contrast-enhanced high-resolution fMRI: Comparison between hemodynamic spread and vascular architecture with CLARITY. *NeuroImage*. Published online August 16, 2017. <https://doi.org/10.1016/j.neuroimage.2017.1008.1046>.
- Ratering, D., Baltes, C., Nordmeyer-Massner, J., Marek, D., and Rudin, M. (2008). Performance of a 200-MHz cryogenic RF probe designed for MRI and MRS of the murine brain. *Magn. Reson. Med.* 59, 1440–1447.
- Schaefer, A., Quinque, E.M., Kipping, J.A., Arélin, K., Roggenhofer, E., Frisch, S., Villringer, A., Mueller, K., and Schroeter, M.L. (2014). Early small vessel disease affects frontoparietal and cerebellar hubs in close correlation with clinical symptoms—a resting-state fMRI study. *J. Cereb. Blood Flow Metab.* 34, 1091–1095.
- Scheffler, K., and Ehses, P. (2016). High-resolution mapping of neuronal activation with balanced SSFP at 9.4 tesla. *Magn. Reson. Med.* 76, 163–171.
- Scheffler, K., and Lehnardt, S. (2003). Principles and applications of balanced SSFP techniques. *Eur. Radiol.* 13, 2409–2418.
- Schölvinck, M.L., Maier, A., Ye, F.Q., Duyn, J.H., and Leopold, D.A. (2010). Neural basis of global resting-state fMRI activity. *Proc. Natl. Acad. Sci. USA* 107, 10238–10243.
- Schulz, K., Sydekum, E., Krueppel, R., Engelbrecht, C.J., Schlegel, F., Schröter, A., Rudin, M., and Helmchen, F. (2012). Simultaneous BOLD fMRI and fiber-optic calcium recording in rat neocortex. *Nat. Methods* 9, 597–602.
- Segal, S.S., and Duling, B.R. (1989). Conduction of vasomotor responses in arterioles: a role for cell-to-cell coupling? *Am. J. Physiol.* 256, H838–H845.
- Shajan, G., Kozlov, M., Hoffmann, J., Turner, R., Scheffler, K., and Pohmann, R. (2014). A 16-channel dual-row transmit array in combination with a 31-element receive array for human brain imaging at 9.4 T. *Magn. Reson. Med.* 71, 870–879.
- Shmuel, A., and Leopold, D.A. (2008). Neuronal correlates of spontaneous fluctuations in fMRI signals in monkey visual cortex: Implications for functional connectivity at rest. *Hum. Brain Mapp.* 29, 751–761.
- Silva, A.C., and Koretsky, A.P. (2002). Laminar specificity of functional MRI onset times during somatosensory stimulation in rat. *Proc. Natl. Acad. Sci. USA* 99, 15182–15187.

- Silva, A.C., Koretsky, A.P., and Duyn, J.H. (2007). Functional MRI impulse response for BOLD and CBV contrast in rat somatosensory cortex. *Magn. Reson. Med.* *57*, 1110–1118.
- Smith, S.M., Fox, P.T., Miller, K.L., Glahn, D.C., Fox, P.M., Mackay, C.E., Filippini, N., Watkins, K.E., Toro, R., Laird, A.R., and Beckmann, C.F. (2009). Correspondence of the brain's functional architecture during activation and rest. *Proc. Natl. Acad. Sci. USA* *106*, 13040–13045.
- Stevens, R.D., Hannawi, Y., and Sair, H. (2014). Small vessel disease and the resting functional architecture of the brain. *J. Cereb. Blood Flow Metab.* *34*, 1089–1090.
- Stroh, A., Adelsberger, H., Groh, A., Rühlmann, C., Fischer, S., Schierloh, A., Deisseroth, K., and Konnerth, A. (2013). Making waves: initiation and propagation of corticothalamic Ca<sup>2+</sup> waves in vivo. *Neuron* *77*, 1136–1150.
- Tak, S., Polimeni, J.R., Wang, D.J., Yan, L., and Chen, J.J. (2015). Associations of resting-state fMRI functional connectivity with flow-BOLD coupling and regional vasculature. *Brain Connect.* *5*, 137–146.
- van Rooden, S., Goos, J.D., van Opstal, A.M., Versluis, M.J., Webb, A.G., Blauw, G.J., van der Flier, W.M., Scheltens, P., Barkhof, F., van Buchem, M.A., and van der Grond, J. (2014). Increased number of microinfarcts in Alzheimer disease at 7-T MR imaging. *Radiology* *270*, 205–211.
- van Veluw, S.J., Zwanenburg, J.J., Engelen-Lee, J., Spliet, W.G., Hendrikse, J., Luijten, P.R., and Biessels, G.J. (2013). In vivo detection of cerebral cortical microinfarcts with high-resolution 7T MRI. *J. Cereb. Blood Flow Metab.* *33*, 322–329.
- Wang, L., Saalman, Y.B., Pinski, M.A., Arcaro, M.J., and Kastner, S. (2012). Electrophysiological low-frequency coherence and cross-frequency coupling contribute to BOLD connectivity. *Neuron* *76*, 1010–1020.
- Yu, X., Wang, S.M., Chen, D.Y., Dodd, S., Goloshevsky, A., and Koretsky, A.P. (2010). 3D mapping of somatotopic reorganization with small animal functional MRI. *NeuroImage* *49*, 1667–1676.
- Yu, X., Glen, D., Wang, S., Dodd, S., Hirano, Y., Saad, Z., Reynolds, R., Silva, A.C., and Koretsky, A.P. (2012). Direct imaging of macrovascular and microvascular contributions to BOLD fMRI in layers IV–V of the rat whisker-barrel cortex. *NeuroImage* *59*, 1451–1460.
- Yu, X., Qian, C., Chen, D.Y., Dodd, S.J., and Koretsky, A.P. (2014). Deciphering laminar-specific neural inputs with line-scanning fMRI. *Nat. Methods* *11*, 55–58.
- Yu, X., He, Y., Wang, M., Merkle, H., Dodd, S.J., Silva, A.C., and Koretsky, A.P. (2016). Sensory and optogenetically driven single-vessel fMRI. *Nat. Methods* *13*, 337–340.
- Zhu, D.C., Tarumi, T., Khan, M.A., and Zhang, R. (2015). Vascular coupling in resting-state fMRI: evidence from multiple modalities. *J. Cereb. Blood Flow Metab.* *35*, 1910–1920.

## STAR★METHODS

### KEY RESOURCES TABLE

REAGENT or RESOURCE	SOURCE	IDENTIFIER
<b>Antibodies</b>		
Anti NeuN antibody	Merck	RRID: AB_2298772, Cat# MAB377
Secondary antibody (Goat Anti-Mouse)	Abcam	RRID: AB_10680176, Cat# ab97035
<b>Bacterial and Virus Strains</b>		
AAV5.Syn.GCaMP6f.WPRE.SV40	PENN Vector Core	Cat# AV-5-PV2822
<b>Chemicals, Peptides, and Recombinant Proteins</b>		
Isoflurane	CP-Pharma	Cat# 1214
Iron oxide nanoparticle: Molday ION	BioPhysics Assay Laboratory (BioPAL)	Cat# CL-30Q02-2
$\alpha$ -chloralose	Sigma-Aldrich	Cat# C0128-25G;RRID
pancuronium bromide	Inresa Arzneimittel	Cat# 34409.00.00
VECTASHIELD Antifade Mounting Medium with DAPI	Vector Laboratories	RRID: AB_2336790, Cat# H-1200
Phosphate Buffered Saline (PBS)	GIBCO	Cat# 10010-023
<b>Experimental Models: Organisms/Strains</b>		
Rat: Sprague Dawley rat	Charles River Laboratories	N/A
<b>Software and Algorithms</b>		
MATLAB	MathWorks	RRID: SCR_001622, <a href="https://www.mathworks.com/">https://www.mathworks.com/</a>
AFNI	<a href="#">Cox, 1996</a>	RRID: SCR_005927, <a href="http://afni.nimh.nih.gov">http://afni.nimh.nih.gov</a>
EEGLAB	<a href="#">Delorme and Makeig, 2004</a>	RRID: SCR_007292, <a href="https://sccn.ucsd.edu/eeglab/index.html">https://sccn.ucsd.edu/eeglab/index.html</a>
Group ICA Of fMRI Toolbox (GIFT)	Medical Image Analysis Lab	RRID: SCR_001953, GIFT 4.0, <a href="http://mialab.mrn.org/software/gift/">http://mialab.mrn.org/software/gift/</a>
Excel 2013	Microsoft	<a href="https://products.office.com/en-us/excel">https://products.office.com/en-us/excel</a>
Adobe Illustrator CC	Adobe	RRID: SCR_010279, <a href="http://www.adobe.com/products/illustrator.html">http://www.adobe.com/products/illustrator.html</a>
<b>Other</b>		
Biopac MP 150 System	Biopac	RRID: SCR_014829
AcqKnowledge Software	Biopac	RRID: SCR_014279, <a href="https://www.biopac.com/product/acqknowledge-software/">https://www.biopac.com/product/acqknowledge-software/</a>
Master-9	A.M.P.I	N/A
Nanoliter Injector	World Precision Instruments	Cat# NANOFIL
Laser (473 nm)	CNI	Cat# MBL-III
Dichroic mirrors	AHF Analysentechnik	Cat# F48-487
Fiber launch	Thorlabs	Cat# MBT613D/M
Optical fiber	Thorlabs	Cat# FT-200-EMT
Optical power meter	Thorlabs	Cat# PM20A
Optical filter	AHF Analysentechnik	Cat# F37-516
Silicon photomultiplier	SensL	Cat# MiniSM-10035-X08
Voltage amplifier	Femto	Cat# DHPVA-100
Tungsten Microelectrode	FHC	Cat# UEWSDDSMCN1M

### CONTACT FOR REAGENT AND RESOURCE SHARING

Further information and requests for resources and reagents should be directed to and will be fulfilled by the Lead Contact, Dr. Xin Yu ([xin.yu@tuebingen.mpg.de](mailto:xin.yu@tuebingen.mpg.de)).

## EXPERIMENTAL MODELS AND SUBJECT DETAILS

### Animals

All experimental procedures were approved by the Animal Protection Committee of Tuebingen (Regierungspräsidium Tuebingen) and performed in accordance with the guidelines. Thirty-five male Sprague-Dawley rats were employed in all experiments. Litter-mates of the male rats (age: 2 - 3 months) were randomly assigned to experimental groups. Both evoked and resting-state bSSFP-fMRI data with A-V maps were acquired from five of nine rats under alpha-chloralose anesthesia, of which both BOLD and CBV signals were acquired under the same A-V map. To verify the effect of different drugs on vascular dynamic network connectivity, five rats were utilized for resting-state BOLD bSSFP-fMRI data under isoflurane anesthesia. In addition, the rats (BOLD: seven of eight, CBV: four of eight) with calcium indicator were employed for the statistics of simultaneous BOLD/CBV rsfMRI and fiber-optic calcium recording studies. Some rats were excluded from statistical analysis due to the large SSFP image distortion introduced by the optical fiber insertion. In addition, seven rats were employed to acquire simultaneous local field potential (LFP) and calcium signal.

### Human Subjects

All human subject experiments follow the guidelines of the regulation procedure in the Max Planck Institute, and the informed consents were obtained from all human volunteers. For 3T MRI image acquisition, six healthy adult subjects (female,  $n = 3$ ; male,  $n = 3$ ; age: 20 - 35 years) were employed to obtain rsfMRI. For 9.4T MRI image acquisition, six healthy adult subjects (female,  $n = 2$ ; male,  $n = 4$ ; age: 20 - 35 years) were examined with Echo-planar imaging (EPI) sequence.

## METHODS DETAILS

### Animal experiments

#### Animal preparation

All procedures were described in a previous study (Yu et al., 2010). Rats were initially anesthetized with isoflurane (5% induction, 1.5% maintenance). Each rat was orally intubated and placed on a mechanical ventilator (SAR-830/AP, CWE). Plastic catheters were inserted into the right femoral artery and vein to allow monitoring of arterial blood gasses and administration of anesthetics. Two different anesthesia treatments were delivered during fMRI (Table S3). For alpha-chloralose anesthesia, after surgery, each rat was given an intravenous bolus of  $\alpha$ -chloralose (60 mg/kg) and isoflurane was discontinued. Anesthesia was maintained with two constant infusion rates of  $\alpha$ -chloralose (15 and 26.5 mg/kg/hr) in combination with pancuronium bromide (4 mg/kg/hr) to reduce motion artifacts. For isoflurane anesthesia, the ventilator maintained the rats breathing under isoflurane 1.2% in the magnet. The rats' rectal temperature was maintained at around 37°C. To prevent head motion, rats were secured in a head holder with a bite bar. All relevant physiological parameters (end-tidal CO<sub>2</sub>, rectal temperature, heart rate, and arterial blood pressure) were continuously monitored during imaging (Figure S3, blood pressure and heart rate). The pulse sequence-based trigger and stimulation control were established using the BioPac system (Goleta, USA) and Master-9 A.M.P.I system (Jerusalem, Israel).

#### Viral vector injection and optical fiber implantation

The viral vectors (AV-1-PV2822 AAV5.Syn.GCaMP6f.WPRE.SV40) were procured from University of Pennsylvania Vector Core (Chen et al., 2013). Viral vectors were injected in the barrel cortex (BC) or the forepaw region of the primary somatosensory cortex (S1FL) of 3 to 4 week old rats. For the stereotactic injection procedure, rats were initially anesthetized with isoflurane. After exposing the skull, a small bur hole was drilled. A nanoliter injector (WPI, FL) was used to place a 35-gauge needle at the proper coordinates in the stereotactic frame. Injections were performed slowly over 5–6 min and the needle was slowly removed after being kept in the injection site for 10 min after finishing the injection. The injection sites of BC were as follows with stereotactic coordinates: AP =  $-2.35$  mm; ML: 4.8 mm; DV = 2; injections each 400 nL at 1.2 mm and 0.7 mm. The injection sites of S1FL were as follows: AP = 0.2 mm; ML = 3.7 mm; DV = 2 injections each 400 nL at 1.2 mm and 0.7 mm. After 6–8 weeks of viral expression, a 200- $\mu$ m optical fiber (7 m length) was inserted through the burr holes on the skull into the BC (stereotactic coordinates: AP =  $-2.7$  mm; ML = 5.1 mm; DV = 1.3 mm; tilt, 4°) or S1FL (AP = 0.2 mm; ML = 4 mm; DV = 1.3 mm). The optical fiber was fixed on the skull with glue. Then, the skin was sutured to cover the glue with the optical fiber extending outside of the rat head.

#### Simultaneous rsfMRI and calcium recording

The optical setup for calcium signal recording was built up based on a previous study (Schulz et al., 2012; M.W., Y.H., T.J. Sejnowski, and X.Y., unpublished data). As shown in Figure S4A, a 473 nm laser (MBC-III, CNI) was set to deliver the fluorescent excitation light. The laser beam was first aligned by a reflection mirror to a correct angle better deflect off a dichroic beam-splitting mirror (BS R488: reflection 471 - 491 nm, >94%; transmission 500 - 1200 nm, >93%; AHF Analysentechnik), which was coupled into a multimode fiber (FT200EMT: NA = 0.48, 230  $\mu$ m cladding diameter; Thorlabs) via amplifying lens (RMS4X; Thorlabs). Fluorescence excitation occurred in the vicinity of the fiber tip inside the MRI scanner and the emitted fluorescence light was collected and guided back to the optical setup through the same fiber. The emitted fluorescent signal from the fiber passed a lens, dichroic mirror, and an emission filter (Semrock RazorEdge; 488 Long Pass; AHF Analysentechnik), and was finally focused by a tube lens (AC254-030-A1-ML; Thorlabs) onto a peltier-cooled silicon photomultiplier with transimpedance preamplifier (MiniSM-10035-X08; SensL). The signal from the photomultiplier was amplified by voltage amplifier (DHPVA-100; Femto) and acquired by the analog input module of a Biopac

MP 150 system (5-K sampling rate). Triggers from the MRI scanner were also recorded by the Biopac system and used to synchronize calcium to BOLD fMRI offline. Laser intensity was measured at the fiber tip for neuronal calcium ( $\sim 5$   $\mu$ W) to avoid phototoxicity for long-term recording by optical power meters (PM20A; ThorLabs).

#### **Simultaneous calcium with electrophysiology recording**

The anesthetized rats were adapted in a stereotaxic device for *in vivo* recordings using similar anesthetics and surgical preparation to the fMRI experiments. Tungsten microelectrode (1 M $\Omega$ ,  $\sim 100$   $\mu$ m, Tungsten, FHC) was bonded to an optical fiber with closely contacted fiber optic tip and electrode contacting point. The local field potential (LFP) was recorded through the EEG module of the Biopac system (gain factor, 5,000; band-pass filter, 0.02 - 100 Hz; sample rate, 5,000/s). In addition, calcium data and blood pressure were digitized and recorded with Biopac MP 150 system at a sampling rate of 5 kHz. The spectrogram of LFP was calculated through multi-taper spectral estimation. (Figure 6, and S7, 1 s sliding window with 0.1 s steps, 9 tapers)

#### **MRI image acquisition from rats (14.1T)**

All images from rats were acquired with a 14.1 T/26 cm horizontal bore magnet (Magnex) interfaced to an Avance III console (Bruker). A transmitter surface coil with a 6-mm diameter was used to acquire images.

##### **bSSFP-fMRI**

Balanced Steady-State Free Precession was implemented with the following parameters: TE, 3.9 ms; TR, 7.8 ms; flip angle (FA), 12 $^\circ$ ; matrix, 96  $\times$  128; FOV, 9.6  $\times$  12.8 mm; slice thickness = 400  $\mu$ m; in-plane resolution = 100  $\times$  100  $\mu$ m $^2$ , resulting in one slice repetition time of 1 s. The block design was 2 s stimulation and 28 s inter-stimulus interval. The duration of each trial of rsfMRI was 15 min, and 2 - 5 trails of BOLD/CBV rsfMRI were acquired for each rat. CBV fMRI signals were acquired after intravenous injection of 15 - 20 mg of Fe/kg dextran-coated iron oxide (BioPAL, MA).

##### **Single-vessel MGE imaging in rats**

The imaging protocol was similar with our previous paper (Yu et al., 2016). To recognize individual arterioles and venules, we employed a 2D Multiple Gradient-Echo (MGE) sequence with the following parameters: TR = 50 ms; TE = 2.5, 5, 7.5, 10, 12.5 and 15 ms; flip angle = 40 $^\circ$ ; matrix = 192  $\times$  192; in-plane resolution = 50  $\times$  50  $\mu$ m $^2$ ; slice thickness = 500  $\mu$ m. We averaged the MGE images from the second echo to the fourth echo and created an arteriole-venule (A-V) map, where the venule voxels display as dark dots (blue marks) because of the fast  $T_2^*$  decay but arteriole voxels remain bright (red marks) owing to the in-flow effect (Figure 1A).

#### **MRI image acquisition from humans (3 T)**

All measurements were performed on a 3-T Siemens Prisma with a 20-channel receive head coil. Six healthy adult subjects (female, n = 3; male, n = 3; age: 20 - 35 years) were employed to obtain a BOLD signal using EPI with the following parameters: TR = 1,000 ms; TE = 29 ms; FA = 60 $^\circ$ ; matrix = 121  $\times$  119; in-plane resolution = 840  $\mu$ m  $\times$  840  $\mu$ m; 9 slices with thicknesses of 1.5 mm. Parallel imaging (GRAPPA factor: 3) and partial Fourier (6/8) were employed to accelerate image acquisition. The visual stimulation consisted of a circular black and white checkerboard. For the resting state fMRI, the duration of each trial of rs-fMRI was 15 min with the eyes-closed condition. The Siemens physiologic Monitoring Unit (PMU) was used to monitor the respiration and pulse oximetry simultaneously. Both PMU physiological log files and EPI data contain time tags, which were utilized to synchronize the temporal profile for statistical analysis.

#### **MRI image acquisition from humans (9.4 T)**

All images were acquired with a 9.4-T MRI scanner (Siemens Healthcare, Erlangen, Germany) with a home-built 16-channel transmit/31-channel receive head coil (Shajan et al., 2014). All the imaging protocols follow those of the 3-T scanner but at a higher resolution. Six healthy subjects (female, n = 2; male, n = 4; age: 20 - 35 years) were examined with EPI sequence: TR = 1,000 ms; TE = 22 ms; FA = 50 $^\circ$ ; matrix = 300  $\times$  300; in-plane resolution = 500  $\mu$ m  $\times$  500  $\mu$ m; 9 slices a thicknesses of 0.8 mm. Parallel imaging (GRAPPA factor: 4) and partial Fourier (5/8) were utilized to accelerate image acquisition.

##### **Single-vessel MGE imaging in humans**

We utilized a 2D MGE sequence with the following parameters: TR = 61 ms; TE = 5.99, 10.39, 14.79, 19.19, 23.59, 27.99, 32.39, 36.79, 41.19, 45.59 ms; flip angle = 60 $^\circ$ ; matrix = 896  $\times$  896; in-plane resolution = 19  $\times$  19  $\mu$ m $^2$ ; slice thickness = 1,000  $\mu$ m. An arteriole-venule (A-V) map was acquired by averaging of the MGE images from the second echo to the ninth echo (Figure 8A).

#### **Data processing**

All data processing was performed using Analysis of Functional NeuroImages (AFNI) software (Cox, 1996) and MATLAB. The relevant fMRI analysis source codes can be downloaded through <https://www.afni.nimh.nih.gov/afni/>. A detailed description of the processing procedure conducted is provided in a previous study (Yu et al., 2012). To register the single-vessel functional map with the A-V map, the tag-based registration method was applied, which carried out ten to twelve tags (venule voxels) of the averaged bSSFP fMRI images corresponding to those of the A-V map. No additional smoothing step was applied. For evoked fMRI analysis, images were normalized by scaling the baseline to 100. Linear regression analysis was applied to estimate the hemodynamic response function. The beta estimates were used to indicate the amplitude of the BOLD response in the beta maps.

### Definition of the individual vessel

The individual vessel voxels in A-V map were identified by the following algorithm: the intensities of arteriole/artery voxels are higher than the mean signal intensities plus two times the standard deviation (s.d.) of the local area in a  $5 \times 5$  kernel, while the intensities of venule/vein voxels are lower than the mean signal intensities minus two times the s.d. of local area, as shown in [Figure 1A](#) (Yu et al., 2016). The locations of individual vessel voxels defined in the A-V map were employed to extract the time courses from BOLD/CBV fMRI of individual vessels.

### Resting state fMRI analysis

The preprocessing analysis was performed using a modified AFNI resting state fMRI processing protocol (afni\_proc.py). The time courses of the vessel seed voxels were chosen for correlation analysis. The vessel voxels from both arteriole and venules were determined based on the A-V map. The detailed image processing procedure utilized was described previously (Yu et al., 2016). Then the 3dTCorr1D function in AFNI was employed to generate the correlation map. In addition, ICA analysis was also performed to characterize the vessel specific correlation maps with the Independent Component Analysis (ICA) Toolbox (GIFT 4.0, MIND Research Network). The ICA toolbox employed principal component analysis (PCA) to realign the data at a lower dimensionality (or reduced variance in a simplified dimensional space). ICA was utilized to generate ten independent components using Infomax algorithms, which specialize in the separation of super-Gaussian sources (Bell and Sejnowski, 1995). After the back reconstruction step, the spatial maps and time courses of components were scaled using Z-scores. Finally, a RETROICOR algorithm (Glover et al., 2000) was implemented to correct physiological motion effects ([Figure S8](#)).

### Power spectrum analysis

Depending on data format, power spectrum analysis was performed in AFNI (image format) or MATLAB (text format). In AFNI, a 3dPeriodogram function was utilized to compute the power spectrum of time courses in all individual voxels. Then the averaged power spectral density was calculated in venule voxels or arteriole voxels, respectively (FFT length: 256, [Figures S6B](#) and [S6D](#)). In MATLAB, we employed Fast Fourier Transform (FFT) to calculate the power spectral density of the physiologic data (respiration/pulse oximetry) ([Figure S8F](#)) and calcium data ([Figure S6F](#)). The calcium signals under light/deep anesthesia were sampled at 1 Hz and calculated by Welch's power spectral density estimate method (FFT length: 256, the overlap: 50%).

### Coherence analysis

Previously, coherence analysis was implemented to identify the functional connectivity between different brain areas (Drew et al., 2008; Wang et al., 2012). For this study, to investigate the interactions of paired vessels, coherence analysis was employed as an indicator of functional interactions and indicator of how well the seed vessel corresponds to other vessel voxels at different frequency ranges. The definition of coherence is as follows:

$$Coh_{xy}(f) = \frac{|P_{xy}(f)|^2}{P_{xx}(f)P_{yy}(f)}$$

where  $x$  indicates the fMRI signal from one seed vessel,  $y$  represents the fMRI time course from another vessel.  $P_{xx}(f)$  and  $P_{yy}(f)$  are the power spectral densities of  $x$  and  $y$ , respectively, and  $P_{xy}(f)$  is the cross power spectral density of  $x$  and  $y$ . The coherence was calculated by using Welch's overlapped averaged periodogram method with FFT (256-point length) and a 256 s Hamming window, which divides  $x$  and  $y$  into equal overlapping sections (240-point overlap, >90% overlap). The frequency resolution of coherence is  $1 / 256 \text{ s} = 0.0039 \text{ Hz}$  which provides enough resolution to observe the slow frequency range.

### The calcium data analysis

The calcium signal was down-sampled to one TR per sample. Next, zero-phase digital filtering (0.01 - 0.1 Hz) was employed to obtain the slow fluctuation of the calcium signal (filtfilt function in MATLAB). In addition, a cross-correlation between the slow fluctuation of the calcium signal and individual venules was performed using the MATLAB function xcorr ([Figures 4E](#) and [4L](#)). A 3ddelay function from the AFNI library was utilized to estimate the time lag map between the slow fluctuation of the calcium signal with BOLD fMRI of venules ( $CC > 0.25$ ) ([Figure 4C](#), inset) or CBV fMRI of arterioles ( $CC < -0.25$ ) ([Figure 4J](#), inset). For the spectrogram of the calcium signal, a function timefreq from EEGLAB (Delorme and Makeig, 2004) was employed to get the averaged power of the spontaneous calcium spikes ([Figures 5B](#) and [6A](#)). A time-varying power spectrogram of calcium signal was computed by using the discrete Fourier transform with a sliding Humming window. The sliding window was 1000 ms without overlap to match one TR of BOLD fMRI data.

### Immunohistochemistry

After the conclusion of the fMRI experiments, the rat brain tissues were perfused using a 4% paraformaldehyde fixative. The tissues were then transferred to 15% sucrose in PBS and kept overnight at 4°C. Next, the prefixed tissues were moved to 30% sucrose in PBS. After sinking, the tissues were stored at -80°C until use. The tissues were also utilized to prepare coronal sequential brain sections (30- $\mu\text{m}$  thickness, -20°C using Leica CM3050S microtome). The sections were incubated overnight at 4°C with primary antibodies: mouse anti-NeuN (1:200; Merck). Afterward, sections were washed five times with PBS and incubated for 60 min with the secondary antibodies: goat anti-mouse conjugated with CY3 (1:500; Abcam). Finally, mounting medium with DAPI (VectaShield, vector) was utilized to protect the fluorescence signal and reveal nuclei. The expression position of GCaMP was confirmed by colocalization with NeuN using a fluorescence microscope (ApoTome, Zeiss).

## QUANTIFICATION AND STATISTICAL ANALYSIS

A paired Student's *t* test was performed to compare the coherence values of paired venules/veins and paired arterioles/arteries in the rat and human resting-state fMRI data. The data with error bars are displayed as the means  $\pm$  SEM. The *p* values  $< 0.05$  were considered statistically significant. The sample size for animal experiments was not previously estimated. The sample size for human experiments was estimated based on the statistical parameters derived from the animal data using  $G^*$  power analysis. No blinding and randomization design was needed in this work.